Magnetic Resonance Tissue Quantification Using Optimal Pulse Sequence Design

By

Zhuo Zheng, B.Eng.

A Thesis
Submitted to the School of Graduate Studies
in Partial Fulfillment of the Requirements
for the Degree
Master of Applied Science

McMaster University

MASTER OF APPLIED SCIENCE(2005)   McMaster University
COMPUTING AND SOFTWARE   Hamilton, Ontario

TITLE: Magnetic Resonance Tissue Quantification Using Optimal Pulse Sequence Design

AUTHOR: Zhuo Zheng, B.Eng. (Wuhan University)

SUPERVISOR: Dr. Christopher Anand and Dr. Tamás Terlaky

NUMBER OF PAGES: xi, 90

Abstract

We present a method for tissue quantification at a resolution that would not be possible for either conventional Dixon method or MR spectroscopy. Our objective is to design a steady-state free precession (SSFP) pulse-sequence which maximizes the contrast to noise ratio in tissue segmentation by solving a nonlinear, nonconvex semi-definite optimization problem. To solve the problem a grid search is used to get a good starting point, and then a sequential, semi-definite trust-region method is developed. The subproblems in our algorithm contain only linear, second order, and semi-definite constraints. Our method can easily be adapted to other pulse sequence types, and it can handle any numbers of tissues and images. As an illustration, we show how the pulse sequences designed numerically could be applied to the problem of quantifying intraluminal lipid deposits in the carotid artery.

We also consider the case where the main magnetic field is not homogeneous, for which we first present a heuristic by adjusting RF pulse phase cycling to correct for the field inhomogeneity. Then we construct a total variation regularization based model, from which we extract two subproblems - field inhomogeneity estimation and tissue density estimation that can be interleaved iteratively. The computational and numerical results show that the model yields a good estimate of both field inhomogeneity and tissue density.

Acknowledgements

Contents

List of Figures

x

List of Tables

Chapter 1

Introduction

We address an MR pulse sequence design problem in order to achieve better resolution and contrast to noise ratio (CNR) in tissue quantification by using nonlinear optimization techniques both in the design of optimal experiments and in image reconstruction. This work was motivated by the fact that currently most clinical imaging methods focus on qualitative imaging, although quantitative applications do exist, especially in functional imaging, e.g., flow measurements in arteries or brain activity. The dynamical system for our imaging pulse sequence design problem was originally developed by Hargreaves et al., [Hargreaves et al., 2001]. However, we have extended that model and developed an approach to quantify different tissue types that outperforms existing methods in terms of both imaging time and resolution. The novelty of our approach comes principally from

- an estimate for CNR in tissue segmentations;

- a method of maximizing CNR using semidefinite optimization (SDO);

- a model for image reconstruction in the presence of main magnetic field inhomogeneity, using total variation (TV) regularization.

The thesis contains five chapters with three main topics, namely, the basics of MRI, tissue quantification using optimal SSFP pulse sequence design, and total variation model-based tissue density and field map estimation. Although MRI is a fairly complex system, in which a tremendous amount of mathematics, physics as well as biochemistry is involved, the reader does not have to have all background knowledge to appreciate this thesis. We have attempted to make this thesis self-contained and accessible to a general audience by giving a short introduction to MRI in the following sections of this chapter,

covering those concepts that are needed to understand our problem. In Chapter 2, tissue separation via a generalized Dixon Method will be discussed and a new nonlinear semi-definite optimization model introduced. Then we take into account the magnetic field inhomogeneity and describe a novel heuristic for estimating field inhomogeneity that further leads to a semi-infinite optimization problem in Chapter 3. In Chapter 4, we give an overview of the total variation (TV) model that will be used for the estimation of tissue densities and field inhomogeneities. We present the results of numerical simulation in Chapter 5. In Chapter 6, we summarize our results and outline some suggestions for future work. The detailed nonlinear semi-definite optimization algorithm is presented in Appendix A.

1.1   MRI Basics

Magnetic Resonance Imaging is a tomographic imaging technique that produces images of internal physical and chemical characteristics of an object from externally measured nuclear magnetic resonance (NMR) signals [Liang and Lauterbur, 1999]. The concept of MRI was introduced in 1973 in the landmark papers of Lauterbur, Mansfield and Grannell [Lauterbur, 1973; Mansfield and Grannell, 1973]. Interest in this field is still growing, due to the fact that MRI is capable of measuring the internal structure and function of the human body in a noninvasive manner. It is widely used medically for the purpose of diagnosis, treatment monitoring and research. The underlying mechanism of imaging comes from the interaction of a nuclear spin with an external magnetic field as described by the Bloch equation (see equation (1.8)) [Haacke et al., 1999, Ch. 4]. In this section, we will derive this equation and outline its properties, since the models we develop are all based on the Bloch equation.

The hydrogen nucleus possesses an angular momentum, which is often called spin. Although nuclear spin is a property characterized by quantum mechanics, it is often visualized in the classical vector model [Liang and Lauterbur, 1999]. One important property of a nuclear spin is the nuclear magnetism associated when placed in an external magnetic field, which is also the physical foundation of MRI. If we represent the spin by a vector quantity $\vec{\mu}$, when placed in an external magnetic field $\vec{B_0}$ produced by a main magnet along the z direction in the three dimensional coordinate system, i.e., $(\vec{B_0} = B_0\vec{z})$ (see Figure 1.1), according to classical mechanics, then the spin satisfies the equation (1.1):

$$\frac{d\vec{\mu}}{dt} = \gamma\vec{\mu} \times B_0\vec{z}. \tag{1.1}$$

2

Solving this differential equation, we obtain:

$$\mu_{xy}(t) = \mu_{xy}(0)e^{-\sqrt{-1}\gamma B_0 t} \tag{1.2}$$

$$\mu_z(t) = \mu_z(0), \tag{1.3}$$

in which $\mu_{xy}(0)$ and $\mu_z(0)$ are initial values. Equation (1.2) describes a clockwise precession of the xy component of μ about the z-axis. The angular frequency ω_0 of precession known as the Larmor frequency can be determined from the equation

$$\omega_0 = \gamma B_0, \tag{1.4}$$

where γ is a constant known as the gyromagnetic ratio. To describe the col-
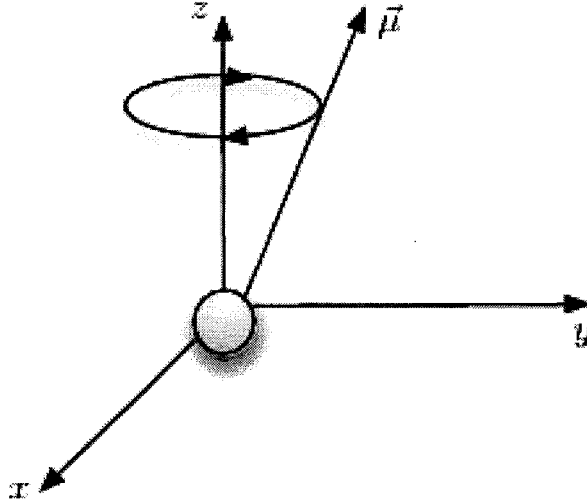
Figure 1.1: The clockwise precession of spin about the direction in which the external magnetic field is assigned.

lective behavior of an ensemble of nuclei present in a specimen or object, we use an aggregate magnetization vector $\vec{M}$, defined as

$$\vec{M} = \sum_{\vartheta=1}^{N} \vec{\mu}_\vartheta, \tag{1.5}$$

in which N is the total number of spins, and $\vec{\mu}_\vartheta$ denotes the ϑth spin in the object. In its equilibrium state $\vec{M_0} = (M_{0,x}, M_{0,y}, M_{0,z})^T$, the magnetization

$\vec{M} = (M_x, M_y, M_z)^T$ is aligned with the direction of the constant external magnetic field. Then we use a radio frequency (RF) pulse that produces an oscillating magnetic field, $\vec{B}_1(t)$, to tip the magnetization away from its equilibrium state down to the transverse plane ($x - y$ plane). In the course of the rotation, the magnetization induces an electric current within a receiver coil appropriately oriented with respect to the same plane. The electric current in the coil is then used to generate a signal. In addition to the RF pulse, there is a system of three orthogonal coils, known as gradient coils, designed to produce time-varying magnetic fields of controlled spatial nonuniformity, which is used for signal localization [Liang and Lauterbur, 1999]. The collected signals are then processed to form an image. We should note that for a single pixel in the reconstructed image, the intensity value depends on a number of parameters that characterize both the constituent tissue types at that pixel and the RF pulse sequence that we used.

Relaxation Times

The response of an isolated proton's spin in an external magnetic field has been modeled by the classical equation of motion of a single magnetic moment (see equation (1.1)), however, the interactions of the proton spin with its neighboring atoms lead to important modifications to this behavior [Haacke et al., 1999, Ch. 4]. After the magnetization has been rotated into the transverse plane, it will tend to grow back along the direction of the static field $\vec{B}_0$ to its equilibrium state. The rate of regrowth can be characterized by a time constant τ_1, called the spin lattice relaxation time, that results from proton interactions with the lattice. Mathematically, the spin lattice relaxation time τ_1 can be determined from the following differential equation:

$$\frac{d\vec{M}_z}{dt} = \frac{1}{\tau_1}(\vec{M}_{0,z} - \vec{M}_z), \qquad (1.6)$$

where $\vec{M}_{0,z} = (0, 0, M_{0,z})^T$ and $\vec{M}_z = (0, 0, M_z)^T$. In the meantime, the combinations of the external magnetic field and the field from the neighbor spins cause individual spins to fan out in time, which results in a reduction of the net magnetization vector. This process is normally called dephasing. Dephasing of spins via spin-spin interaction produces a decay of the individual transverse components (and hence the transverse magnetization) that is characterized by a time constant τ_2, called the spin spin relaxation time:

$$\frac{d\vec{M}_\perp}{dt} = -\frac{1}{\tau_2}\vec{M}_\perp, \qquad (1.7)$$

in which $\vec{M}_\perp = (M_x, M_y, 0)^T$.

Chemical Shift Effect

Hydrogen protons in different molecules are immersed in slightly different magnetic environments, even in the presence of identical external magnetic fields [Liang and Lauterbur, 1999]. Therefore, different chemical compounds have slightly different local magnetic fields which means that the local Larmor frequency is chemically shifted to different values $\omega_0(j)$ depending on the molecular species type j, which is called a resonance offset or chemical shift, because it causes tissues to appear shifted with respect to each other in some types of reconstructed images.

Rotating Frame of Reference

Up to now, we have considered the motion of magnetization in a stationary coordinate system. A rotating frame is a coordinate system whose transverse plane is rotating clockwise at an angular frequency. Since the RF coil generates a magnetic field at a frequency that matches that of the spin system's precession in order to achieve resonance, it would be much easier for the computation if we consider the precession in a rotating coordinate system that rotates at an angular frequency ω_0. The benefit of using such a rotating frame of reference will become clear in section (1.2) and further in Chapter 3.

Bloch Equation

Taking into account the motion of a spin system in a pure external magnetic field $\vec{B}_0$, as well as the effects of spin lattice and spin spin relaxation after the application of the RF pulse, we arrive at an equation that quantitatively describes the time-dependent behavior of the magnetization $\vec{M}$ in the presence of $\vec{B}_0$ and $\vec{B}_1(t)$. By combining equation (1.1) with relation (1.5) that allows to replace $\vec{\mu}$ by $\vec{M}$, and taking into account equations (1.6), and (1.7), we arrive at the Bloch equation:

$$\frac{d\vec{M}}{dt} = \gamma \vec{M} \times \vec{B}_0 + \frac{1}{\tau_1}(\vec{M}_{0,z} - \vec{M}_z) - \frac{1}{\tau_2}\vec{M}_\perp. \qquad (1.8)$$

MRI measures the aggregate magnetic field generated by the spins of all the protons in the object. Because the number of protons is very large, we can model the proton density as a continuous function, or a piecewise continuous

function [Haacke et al., 1999, Ch. 1 and 4]. It is common to discretize the magnetization by tessellating the region into a regular volume, called voxel, and assigning the sum of the magnetization in each voxel to a point in the discretization. Since tissues of different types have different properties which result in different magnetizations, our voxel model must include the proportions of tissues of different types. The evolution in the magnetization in one voxel is independent of the magnetization in neighboring voxels, hence, we can consider the signal from each voxel separately. Since (1.5) and (1.8) are linear, we can use it to solve for the evolution of each tissue's magnetization separately, and sum up the resulting magnetizations, which is also the underlying idea of our approach for tissue quantification.

1.2   MR Pulse Sequence

As we have mentioned, the RF pulse is a crucial part of the imaging system, because it manipulates the rotation of the magnetization that leads to a measurable signal. Since the motion of the magnetization is the combined result of two perpendicular magnetic fields, the precession of the magnetization follows a spiral trajectory down to the transverse plane when an RF pulse is applied. However, if we observe it in the rotating frame as introduced earlier, the precession about the z axis disappears, since the coordinate system is also precessing at the same angular frequency as the magnetization. The precession of $\vec{M}$ about the $\vec{B}_1$ field generated by RF coil is called forced precession [Liang and Lauterbur, 1999], the angular frequency ω_1 of which in the rotating frame of reference is determined by (see also (1.4)):

$$\omega_1 = \gamma B_1. \tag{1.9}$$

As a consequence of the forced precession, magnetization is flipped from the longitudinal direction along the z axis by a certain angle. The flip angle is defined as the smaller angle between $\vec{M}$ and the z axis [Liang and Lauterbur, 1999].

In MRI, we often use multiple RF pulses to realize different imaging goals. Hence, the repetition time (t_r) between two consecutive pulses is an important issue we need to take care of, because it controls the degree of both spin lattice relaxation and spin spin relaxation. Since MR signal depends on a set of parameters including the relaxation times, variation in t_r would influence the signal, and eventually quality of reconstructed images.

A typical pulse sequence consists of a combination of individual RF pulses with (possibly) different flip angles, for which the time interval between

two consecutive pulses is determined by the repetition time. An overview of pulse sequences itself is an interesting topic with extensive literature [Haacke et al., 1999, Ch. 15], which makes it impossible to be covered here in detail. We restrict our discussion to a specific type of pulse sequence - called steady-state free precession (SSFP) - that is used in our tissue quantification problem.

1.2.1   Steady-State Free Precession

When a spin system is excited by a train of periodic radio frequency (RF) pulses with repetition time $t_r \ll \tau_2$, the spin system will reach a dynamic equilibrium, known as the steady state [Carr, 1958]. One can find several reports about SSFP signal and SSFP pulse sequences in recent years, see e.g., [Hanicke and Vogel, 2003; Hargreaves et al., 2001; Scheffler, 2003]. The popularity of SSFP sequences is due to the advantage that they yield high signal strength in short scan time, high image resolution and good image contrast. For this reason, we use SSFP sequences to demonstrate our method to optimally determine the pulse design parameters that maximize the CNR.

The physical system is well-described by the Bloch equation (1.8), but for our purposes it is simpler to discretize the system by assuming the fixed simple pulse-sequence design shown in Figure 1.2 and integrating the Bloch equation in each section. The magnetization is governed by a dynamical system defined in [Hargreaves et al., 2001]. We will show it has a steady-state which can be found by solving a linear system. To see this, and get a better idea about the constraints we will build up the dynamical system from its components.

The dynamical system is the composition of several simple components, parameterized by the tissue parameters

$$(\tau_1, \tau_2, \kappa) \in \mathbb{R}_+ \times \mathbb{R}_+ \times \mathbb{R}, \tag{1.10}$$

where τ_1, τ_2 are relaxation times of the magnetization measured in milliseconds (ms), κ is the resonance offset of the tissue measured in Hz, $\mathbb{R}_+$ is the set of nonnegative real numbers, and the pulse-sequence design variables

$$(\alpha, f, T) \in \mathbb{R} \times \mathbb{R} \times \mathbb{R}_+, \tag{1.11}$$

where α is the flip angle, f is the angle of RF pulse phase cycling which models the change of the axis of rotation of the RF pulse, T is the echo time which we fix to be half of the repetition time t_r. Fixing the echo time to be midway between RF pulses corresponds to the most basic spin-warp and radial

k-space trajectories [Haacke et al., 1999, Ch. 9]. Other choices of readout trajectories would lead to other fixed ratios. Simultaneously optimizing RF pulse design and readout trajectories would lead to a more complicated optimization problem, which is beyond the scope of this thesis.
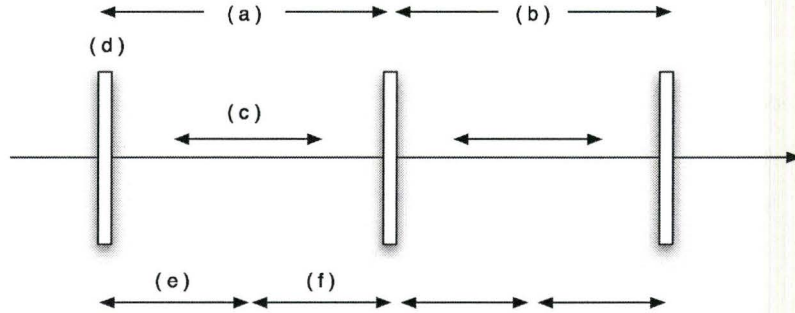
Figure 1.2: SSFP pulse sequence showing two pulse repetitions (a) and (b). Each pulse interval contains one readout interval (c) when data is collected, and one RF pulse (d).

The first component is the rotation of the magnetization vector caused by the RF pulse:

$$R = \begin{pmatrix} 1 & 0 & 0 \\ 0 & \cos(\alpha) & \sin(\alpha) \\ 0 & -\sin(\alpha) & \cos(\alpha) \end{pmatrix}. \tag{1.12}$$

Variations in bulk susceptibility of the different tissues cause different tissue to observe different magnetic fields B, which we capture by the parameter κ, this causes a rotation about the z axis that also depends on the echo time T:

$$P = \begin{pmatrix} \cos(\kappa T) & \sin(\kappa T) & 0 \\ -\sin(\kappa T) & \cos(\kappa T) & 0 \\ 0 & 0 & 1 \end{pmatrix}. \tag{1.13}$$

In designing the pulse sequence, we can change the axis of rotation of the RF pulse referred to as RF pulse phase cycling, because all current generation scanners have the ability to rotate this angle by a fixed constant, which is usually an integral fraction of 2π. To simplify this analysis, it is easier to fix the RF pulse phase, and pretend that the rest of the experiment rotates from

one RF pulse to the next by

$$Q = \begin{pmatrix} \cos(f) & \sin(f) & 0 \\ -\sin(f) & \cos(f) & 0 \\ 0 & 0 & 1 \end{pmatrix}. \qquad (1.14)$$

We collect the effect of relaxation into two components:

$$C = \begin{pmatrix} e^{-T/\tau_2} & 0 & 0 \\ 0 & e^{-T/\tau_2} & 0 \\ 0 & 0 & e^{-T/\tau_1} \end{pmatrix} \qquad (1.15)$$

and

$$D = \begin{pmatrix} 0 \\ 0 \\ \left(1 - e^{-T/\tau_1}\right) \end{pmatrix}, \qquad (1.16)$$

where the scaling of D assumes that $\vec{M}$ has been scaled so that the minimum energy state is $\vec{M_0} = (0, 0, \text{proton density})^T$. We have

$$M_{k+1} = P(C(RQP(CM_k + D)) + D). \qquad (1.17)$$

If a steady-state exists, it satisfies

$$M_{k+1} = M_k = M_{SS}. \qquad (1.18)$$

Therefore,

$$AM_{SS} = b, \qquad (1.19)$$

where $\bar{A} = PCRQPC$, $A = I - \bar{A}$ and $b = PCRQPD + PD$.

Since the rotations R, P, and Q have unit eigenvalues, and all the eigenvalues of the relaxation matrix C are less than one (and positive), the matrix A is invertible, and so the steady state M_{SS} exists, and can be solved either symbolically or numerically for particular values of the parameters.

Chapter 2

Tissue Quantification Using Optimal SSFP Pulse Sequence Design

Tissue quantification, by definition, refers to the problem of estimating different tissue quantities from a region of interest in an image in order to reveal anatomical structures. This is important for many clinical applications, since it provides useful quantitative information about different tissue types regardless of their physical distribution. For example, neurological diseases are normally associated with some abnormalities in brain tissue volumes [Santago and Gage, 1993]. Given the pathological changes observed using MRI, identification of these changes can be achieved in vivo by tissue quantification.

MR images are typically analyzed by qualitative, or semi-qualitative visualization or evaluation [Wang et al., 1998]. Tissue quantification can be approximated by segmentation, where the reconstructed image is subdivided into its constituent regions or objects. In cases where distinct tissue types are well-separated physically, and are large in extent relative to image resolution, quantitative tissue volumes have been successfully extracted from qualitative images by calculations based on manual and automatic contour estimation [Jardim and Figueiredo, 2003]. However, these methods of tissue separation are based on selectively suppressing tissue from undesired components, and they are sensitive to main field inhomogeneity and other conditions. Therefore they are unsuitable for tissues colocated at the image resolution.

An alternative to MRI tissue quantification is MR spectroscopy [Salibi and Brown, 1998], which can be used to quantify multiple molecules in regions of interest. Unfortunately, it is extremely limited in spatial and temporal resolution, and it is at least an order of magnitude slower than imaging

methods.

Due to the various limitations for the existing tissue quantification methods, we introduce our approach in this chapter, which improves on conventional Dixon methods [Glover, 1991; Huang et al., 2004; Reeder et al., 2004; Vasanawala et al., 2000] since it

- does not dictate a particular configuration of phases (*e.g.,* in and out of phase) and look for pulse-sequence design variables to match this configuration,

- takes all tissue parameters into account (relaxation constants, as well as resonance offset),

- can be used to quantify any number of tissues, and

- increases the CNR of images acquired faster than signal averaging–and allows greater latitude in trading off imaging time versus CNR.

These advantages are the direct results of formulating the selection of pulse-sequence design variables as an optimization problem, including the formulation of an objective function which measures the CNR. However, before we get into the technical subtleties, we first introduce the generalized Dixon method, on which our idea of tissue quantification is based.

2.1 Tissue Quantification via a Generalized Dixon Method

2.1.1 Tissue Quantification Prototype

For a sample voxel that consists of m tissue types with concentrations

$$(\rho_1, \rho_2, \ldots, \rho_m) \in \mathbb{R}^m,$$

which is imaged n times by varying the pulse sequence, the resulting signals $(\iota_1, \iota_2, \ldots, \iota_n) \in \mathbb{C}^n$, are given by

$$\iota_1 = a_{11}\rho_1 + a_{12}\rho_2 + \ldots + a_{1m}\rho_m,$$
$$\iota_2 = a_{21}\rho_1 + a_{22}\rho_2 + \ldots + a_{2m}\rho_m,$$
$$\vdots$$
$$\iota_n = a_{n1}\rho_1 + a_{n2}\rho_2 + \ldots + a_{nm}\rho_m,$$

where by definition $\iota_k = M_x(k) + \sqrt{-1}M_y(k)$ is the projection of the magnetization $M_{k\text{th tissue}}$ to the x-y plane, which is identified with the complex plane, and $a_{ij} \in \mathbb{C}$ gives the expected signal in image i of a unit quantity of tissue j. Therefore, the coefficient matrix $S^{\mathbb{C}} = (a_{ij})_{n \times m}$ defines a linear transformation from tissue concentrations to signal measurements. If S is considered as a real matrix having twice the number of rows as the complex coefficient matrix $S^{\mathbb{C}} = (a_{ij})_{n \times m}$ by splitting the real and imaginary parts of a_{ij} into two adjacent rows, and $\text{rank}(S) = m$, then we can invert this linear system to find the tissue concentrations. This is the basic idea of tissue quantification, the interesting part is how to choose pulse-sequence design variables so that S is well-conditioned.

2.1.2 Dixon Method

All imaging methods in MR are based on understanding (and working with) the behavior of solutions of the Bloch equation (1.8). The Dixon Method, [Dixon, 1984], uses chemical differences between tissues which manifest themselves as different external field values, and hence different resonant frequencies. For tissues with different resonant frequencies, the signals will go in and out of phase periodically. Dixon observed that for fat and water, if one image is acquired while both are in phase and one while they have opposite phases, then

$$S^{\mathbb{C}} = \begin{pmatrix} 1 & 1 \\ 1 & -1 \end{pmatrix}, \text{ equivalently, } S = \begin{pmatrix} 1 & 1 \\ 0 & 0 \\ 1 & -1 \\ 0 & 0 \end{pmatrix}, \qquad (2.1)$$

and addition and subtraction of images is all that is required to recover the original fat and water concentrations. The difference between the effective excitation time and the effective measurement time is called the echo time. Dixon fixed the phase relationship by altering the echo time, but ignored differences caused by relaxation. When we formulate the model for SSFP sequences, we will be concerned with repetition time, the time between successive excitation pulses. Repetition time always effects signal generation, but for spoiled pulses, it can be excluded from calculations of the complex phase of the signal, whereas for SSFP, phase in addition to magnitude are very sensitive to repetition times.

This analysis ignores the fact that equal quantities of fat and water may not generate the same magnitude of signal, but this can be calibrated.

The Dixon method usually uses spoiled sequences [Haacke et al., 1999, Ch. 18], because (ignoring the calibration issue) relaxation parameters can be

ignored. For SSFP sequences, relaxation parameters cannot be ignored, and Hargreaves et al., [Hargreaves et al., 2003], adjust the pulse-sequence design variables of SSFP sequences by proper selection of the sequence repetition time and the center frequency offset that makes different tissue types properly go out of phase, respectively, in order to realize a 180° phase difference between fat/water signals. Other authors, *e.g.,* Vasanawala et al., [Vasanawala et al., 2000], have considered more general tissue separation problems, but always with similar simple structures for $S^{\mathbb{C}}$.

Dixon introduced the principle of separating different tissue types by manipulating the phase relationships, which can be easily extended to more cases than fat and water, as shown in our simulation part (see Chapter 5). The linear transformations S used in the Dixon method are simple by design, and therefore usually not written in matrix form. Not doing so, obscured the fact that more general linear combinations of tissue densities can be used for tissue quantification. Recently, Rybicki *et al.,* and Reeder *et al.,* [Reeder et al., 2004; Rybicki, 2001] have considered matrices containing square roots and arbitrary complex roots of unity, respectively. This complex matrix can be approximated by manipulating a single pulse design variable (echo time), when the resonant frequencies of the different tissues are well separated. To the best of our knowledge, we are the first to exploit the generalization to arbitrary complex values. That this has not been discussed before, is perhaps because there was previously no way of evaluating the relative merits of different linear combinations. The introduction of a merit function, and a systematic computational method of optimizing this function over all possible choices of pulse sequence design variables for the case of SSFP pulses are the main contributions of this thesis. Note that Reeder *et al.,* do use noise in the tissue separations as an objective, and discuss the merits of their proposed heuristic for choosing echo times. They find that in the best case, noise in computed tissue separations is reduced as would be expected from signal averaging alone. By optimizing over a larger number of design variables, we observe better than the expected reduction from signal averaging alone.

2.2 Imaging

Based on what has been discussed in Section (2.1), we arrive to the following problem statement: Let m be the number of tissues, and n the number of experiments. We denote $u_l = (u_{1l}, u_{2l}, u_{3l}, u_{4l}, T_l) \in \mathbb{R}^5$, $l = 1, \ldots, n$, $t_k = (\tau_{1k}, \tau_{2k}, \kappa_k) \in \mathbb{R}^3$, $k = 1, \ldots, m$, where we represent the angles α_l and f_l by unit vectors $(u_{1l}, u_{2l}) = (\cos(\alpha_l), \sin(\alpha_l))$ and $(u_{3l}, u_{4l}) = (\cos(f_l), \sin(f_l))$. If

$M_{\mathrm{SS}}(u_l, t_k) \in \mathbb{R}^3$ is the steady state magnetization corresponding to design variables u_l and tissue parameters t_k, with components $M_{\mathrm{SS},x}$, $M_{\mathrm{SS},y}$, $M_{\mathrm{SS},z}$, and ρ_k is the density of tissue k, then the measured signal from experiment l is

$$\left(\sum_{k=1}^{m} M_{\mathrm{SS},x}(u_l, t_k)\rho_k, \sum_{k=1}^{m} M_{\mathrm{SS},y}(u_l, t_k)\rho_k \right).$$

If we write the results of n experiments (*i.e.*, images) as a $2n$ dimensional real vector, and the m dimensional tissue densities as an m dimensional real vector, the transformation from tissue densities to measurements is

$$S = \begin{pmatrix} M_{\mathrm{SS},x}(u_1, t_1) & \ldots & M_{\mathrm{SS},x}(u_1, t_m) \\ M_{\mathrm{SS},y}(u_1, t_1) & \ldots & M_{\mathrm{SS},y}(u_1, t_m) \\ \vdots & \vdots & \vdots \\ M_{\mathrm{SS},x}(u_n, t_1) & \ldots & M_{\mathrm{SS},x}(u_n, t_m) \\ M_{\mathrm{SS},y}(u_n, t_1) & \ldots & M_{\mathrm{SS},y}(u_n, t_m) \end{pmatrix}, \tag{2.2}$$

If S does not have full rank, we cannot reconstruct tissue densities from this set of images. If S does have full column rank, the Moore-Penrose Pseudo-Inverse [Horn and Johnson, 1985] of S, $\left(S^T S\right)^{-1} S^T$, is an unbiased maximum likelihood estimator [Mardia et al., 1979, Thms. 6.2.1, 6.2.2] for the tissue densities as a function of the measured image data. In the next section, we will show how the pulse-sequence design variables can be chosen, not only to avoid singular transformations, but to maximize the quality of the computed tissue densities.

2.3 Semi-definite Optimization Problem

Our objective is to choose the pulse-sequence design variables such that the error in the reconstructed tissue densities is minimized. As is standard practice in MR imaging, we will assume that measurement noise is white, that is, independent and normally distributed [Haacke et al., 1999]. Under this assumption the error in the reconstructed tissue densities will also be normally distributed (since the reconstruction is a linear transformation), but the error in different tissue density components will not necessarily be independent. Barring additional information about the use of tissue segmentation (*e.g.*, the method of diagnosis in which they will be employed), we assume that the objective is to minimize the worst-case error among different tissue densities. Even if in a particular application, we may only be concerned in the quantification of one tissue, it is likely that radiologists would occasionally want to

examine other tissue density images, so minimizing the worst-case error is a good conservative design criterion.

2.3.1   Formulation

Since the Moore-Penrose Pseudo-Inverse [Horn and Johnson, 1985] is a linear map from measured signals to density estimates, it follows that if $\epsilon \in \mathbb{R}^{2n}$ is a vector of measured noise, then the resulting errors in the tissue densities are also normally, but not identically distributed, and given by $\left(S^T S\right)^{-1} S^T \epsilon$.

We can calculate the expected error in the tissue density estimates by using a singular-value decomposition $S = V^T D U$, where V and U are orthonormal and D is diagonal. Then we have

$$(S^T S)^{-1} S^T \epsilon = U^T D^{-1} V \epsilon. \tag{2.3}$$

Since each measurement noise is independent with distribution $N(0, \sigma)$, for any two rows V_i and V_j in the orthonormal matrix V, $V_i \epsilon$ and $V_j \epsilon$ are also independent with distribution $N(0, \sigma)$, which means that each component in $\epsilon' = V\epsilon$ is also independent with distribution $N(0, \sigma)$. Similarly, each component in $\epsilon'' = D^{-1}\epsilon'$ is independent with distribution $N(0, \lambda_i^{-1}\sigma)$, in which, λ_i is the ith singular value of D. When left multiplied by the matrix U^T, the resulting error, $\epsilon''' = U^T \epsilon''$ also has normally distributed components, with the ith element having distribution $N(0, \sigma\sqrt{\sum_j (U_{i,j}^T)^2 \lambda_j^{-2}})$. To minimize the worst-case error, we want to minimize the largest value

$$\sigma\sqrt{\sum_j (U_{i,j}^T)^2 \lambda_j^{-2}},$$

for all values of i. This is equivalent to minimizing the maximal λ_i^{-2}, which is equivalent to maximizing the minimal λ_i. Since

$$S^T S = U^T D V V^T D U = U^T D^2 U,$$

and the eigenvalues of D^2 and $U^T D^2 U$ coincide because $U^T U = I$, the eigenvalues of D^2 are the same as the eigenvalues of $S^T S$. Thus our goal is to

$$\max_{\text{design variables}} \min\{\text{eigenvalues of } S^T S\}. \tag{2.4}$$

We formulate the eigenvalue optimization problem (2.4) using semidefinite inequalities as

$$\max \lambda$$
$$S^T S - \lambda I \succeq 0,$$

where $\succeq 0$ means that the matrix on the left hand side of the inequality has to be square, symmetric and positive semi-definite. Additional constraints for S and for the design variables describe the set of feasible design variables.

The formulation of the constraints involves three angles that always occur as sine-cosine pairs, which define rotations around two of the coordinate axes in $\mathbb{R}^3$. We can replace the sines and cosines that appear in the rotation matrices R and Q by unit vectors (see p.24.) u_{1l} and u_{2l}, and add the constraints

$$u_{1l}^2 + u_{2l}^2 = 1, \tag{2.5}$$
$$u_{3l}^2 + u_{4l}^2 = 1. \tag{2.6}$$

We can then relax the constraints (2.5) and (2.6) to the convex quadratic constraints

$$u_{1l}^2 + u_{2l}^2 \leq 1, \tag{2.7}$$
$$u_{3l}^2 + u_{4l}^2 \leq 1. \tag{2.8}$$

Although we do not have a proof, we expect that the relaxed problem is equivalent to the original problem, so we can solve the relaxed problem, and check that the constraints (2.5) and (2.6) are satisfied (within numerical tolerance). We reason the equivalence as follows: Scaling a unit vector $(u_{1l}, u_{2l})^T$ or $(u_{3l}, u_{4l})^T$ to lie strictly inside the unit disk will have the effect of increasing the norm of A, (see (1.19)), which will, in general, decrease the norm of M_{SS}, (see (1.19)). This will scale the row of S corresponding to that experiment, which will, in general, reduce the minimum eigenvalue of $S^T S$, and hence reduce the objective function.

In addition to the angles, we have variables T_l, which control the repetition time of the pulse sequence used to collect an image. In practical applications, this variable is bounded below by hard physical constraints on the instrumentation ($T_{\min}$), and it is bounded above by practical limits on SSFP image stability ($T_{\max}$), and limits on the patients ability to remain still (possibly including holding their breath). (These limits also depend on the particular model of imager, on the part of the body being imaged, and the field strength of the magnet.) Since the original Dixon methods used echo time alone to differentiate fat and water [Dixon, 1984], we expect our objective to be very sensitive to variations in T_l between experiments.

2.3.2 Complete System

Recall that m stands for the number of tissues and n stands for the number of experiments, and

$$A(u_l, t_k) =$$
$$\quad I - P(T_l, \kappa_k)C(T_l, \tau_{1k}, \tau_{2k})R(u_{1l}, u_{2l})Q(u_{3l}, u_{4l})P(T_l, \kappa_k)C(T_l, \tau_{1k}, \tau_{2k}),$$
$$b(u_l, t_k) =$$
$$\quad (P(T_l, \kappa_k)C(T_l, \tau_{1k}, \tau_{2k})R(u_{1l}, u_{2l})Q(u_{3l}, u_{4l}) + I)P(T_l, \kappa_k)D(T_l, \tau_{1k}),$$

and

$$S(u_1, \ldots, u_n, t_1, \ldots, t_m) = \begin{pmatrix} M_{\text{SS},x}(u_1, t_1) & \ldots & M_{\text{SS},x}(u_1, t_m) \\ M_{\text{SS},y}(u_1, t_1) & \ldots & M_{\text{SS},y}(u_1, t_m) \\ \vdots & \vdots & \vdots \\ M_{\text{SS},x}(u_n, t_1) & \ldots & M_{\text{SS},x}(u_n, t_m) \\ M_{\text{SS},y}(u_n, t_1) & \ldots & M_{\text{SS},y}(u_n, t_m) \end{pmatrix}. \tag{2.9}$$

Using this notation, we can now write the entire optimization model in the compact form:

$$\begin{aligned} \max \quad & \lambda \\ \text{s.t.} \quad & S^T S - \lambda I \succeq 0 \\ & A(u_l, t_k)M_{SS}(u_l, t_k) = b(u_l, t_k) \quad \forall l, k \\ & u_{1l}^2 + u_{2l}^2 \leq 1 \quad \forall l \\ & u_{3l}^2 + u_{4l}^2 \leq 1 \quad \forall l \\ & T_{\min} \leq T_l \leq T_{\max}, \end{aligned} \qquad \text{(NL-SDO)}$$

where $l = 1, \ldots, n$, $k = 1, \ldots, m$. Note that in the nonlinear semi-definite optimization problem (NL-SDO), constraints $u_{i,l}^2 + v_{i+1,l}^2 \leq 1, \forall l, i = 1, 3$ are second order cone constraints (SOCO), see [Ben Tal and Nemirovski, 2001].

This is a nonlinear, nonconvex semi-definite optimization problem. An optimal solution corresponds to optimal design variables of the SSFP pulse sequence, from which we can achieve tissue density estimation with good CNR (see Chapter 5). However, the quality of the estimate is still influenced by some other factors, such as magnetic field inhomogeneities. To design a robust pulse sequence, we have to address the problem of correcting field inhomogeneities, which will be our focus in the next two chapters.

Chapter 3

Tissue Quantification in the Presence of Field Inhomogeneity

In this chapter we explore the problem of quantifying tissue types in the presence of main magnetic field inhomogeneity, by examining the structure of the dynamical model. A heuristic will be presented based on the mathematical derivation of the equivalence (within measurement error) between the effect of field inhomogeneity and a shift of RF pulse phase cycling. Furthermore, we also formulate a semi-infinite optimization problem in order to compensate field inhomogeneity. Our aim is to design robust pulse sequences.

From what has been discussed, we know that for magnetic resonance imaging, highly uniform magnetic fields are necessary because they determine the frequency at which the magnetization resonates, and this frequency determines position, complex phase as well as M_{SS} in MR imaging. In practice, however, there always exist magnetic field inhomogeneities for a variety of reasons. For example, imperfections within the main magnetic field generating magnet due to design and manufacturing. Different magnetic susceptibility of materials may also cause the inhomogeneities at the regions where the materials come into contact such as air/tissue interfaces. As a consequence, field inhomogeneities can lead to geometric distortions and other artifacts in reconstructed images.

The extent to which field inhomogeneities impair the image quality is determined by many factors, such as the severity of inhomogeneity, sensitivity

of the imaging sequence type, length of repetition time, etc. Unfortunately, steady-state free precession (SSFP) imaging that we have studied for tissue density estimation in our model is quite sensitive to field inhomogeneity. For example, dark stripe artifacts are common in SSFP imaging as a manifestation of off-resonance caused by field inhomogeneities [Li et al., 2004]. The reason behind the phenomenon can be understood through a simple analysis based on our imaging model. The resonant frequency ω_0 at which the magnetization precesses depends bilinearly on two factors: the gyromagnetic ratio γ and the main magnetic field B_0 ($\omega_0 = \gamma B_0$). Consider a field inhomogeneity ΔB_0 at a certain point on image, during the time interval $\Delta\varphi$ between two consecutive pulses. The magnetization accumulates the extra angular phase $\psi = \gamma \Delta B_0 \Delta\varphi$ during the precession. Because ΔB_0, and hence ψ are position-dependent, different dephasing may be observed at different spatial locations. To further illustrate our point, we numerically simulate the impact of dephasing within the range of $[-2\pi, 2\pi]$ caused by field inhomogeneities on the expected noise (minimum singular value of S) in the reconstructed tissue densities in Figure 3.1. If we also take into account the chemical shift effect $\Delta\gamma$ that results from the slightly different magnetic environments in which proton spins in different molecule are immersed, we can characterize the rotation of different tissue types due to variations in bulk susceptibility as:

$$\check{P} = \begin{pmatrix} \cos\left((\gamma + \Delta\gamma)(B_0 + \Delta B_0)T\right) & \sin\left((\gamma + \Delta\gamma)(B_0 + \Delta B_0)T\right) & 0 \\ -\sin\left((\gamma + \Delta\gamma)(B_0 + \Delta B_0)T\right) & \cos\left((\gamma + \Delta\gamma)(B_0 + \Delta B_0)T\right) & 0 \\ 0 & 0 & 1 \end{pmatrix}.$$

Since we are modelling the dynamical system in a rotating frame of reference, we can ignore the γB_0 term (recall that the coordinate system is precessing at the resonance frequency $\omega_0 = \gamma B_0$); the chemical shift effect $\Delta\gamma$ is very small, when multiplied by a field inhomogeneity ΔB_0, $\Delta\gamma \Delta B_0$ becomes a negligible term that can be ignored without seriously affecting the result because it is smaller than any other term by at least on the order of 10^{-6}; note also that chemical shift factor $\Delta\gamma$ is what induces the tissue susceptibility variation, hence $\kappa = \Delta\gamma B_0$. Taking the above discussion into account, we focus on the terms inside the trigonometric functions in the matrix $\check{P}$:

$$\begin{aligned} \tilde{P} &= \check{P}(((\gamma + \Delta\gamma)(B_0 + \Delta B_0) - \gamma B_0)T) \\ &= \check{P}((\underbrace{\Delta\gamma B_0}_{\kappa} + \gamma \Delta B_0 + \Delta\gamma \Delta B_0)T) \\ &\approx \check{P}((\kappa + \gamma \Delta B_0)T) \end{aligned}$$

20

Therefore,

$$
\tilde{P} = \begin{pmatrix} \cos\left((\kappa + \gamma \Delta B_0)\, T\right) & \sin\left((\kappa + \gamma \Delta B_0)\, T\right) & 0 \\ -\sin\left((\kappa + \gamma \Delta B_0)\, T\right) & \cos\left((\kappa + \gamma \Delta B_0)\, T\right) & 0 \\ 0 & 0 & 1 \end{pmatrix}, \qquad (3.1)
$$

where ΔB_0 can be calibrated by a field map.

Since field inhomogeneity may cause serious problems [Haacke et al., 1999, Ch. 20], much research has been done on field inhomogeneity correction in the past. Generally speaking, there are two steps involved in most field inhomogeneity rectification schemes. The first is to measure spatial variation of the magnetic field (referred to as 'estimating the field map'). The second step is the use of that field map to compensate field inhomogeneities during the reconstruction step. Some methods have been developed that combine the two steps [Nayak and Nishimura, 2000]. In order for the readers to better understand our approach, we first present our formation for the field compensation problem in this chapter, and leave the field mapping problem for Chapter 4.

3.1 Semi-infinite Problem

Our objective is to design robust pulse-sequences to withstand the perturbation of magnetic field inhomogeneities over a certain range. Suppose that $\Delta B_0 \in [\Delta B_{0,\min}, \Delta B_{0,\max}]$ is the magnitude of the magnetic field inhomogeneity at a certain pixel we are dealing with. In other words, if we denote each possible value of the field inhomogeneity as ΔB_0 within the interval, then ΔB_0 may take on infinite number of values. Theoretically, to minimize the expected noise of that pixel in the reconstructed tissue densities, we should solve an optimization subproblem that gives the best - worse - noise among all ΔB_0 values. Recall (see Section 2.3.2) that k is the tissue parameter index, and l is the experiment index,

$\tilde{A}(u_l, t_k, \gamma_k \Delta B_0) =$

$\quad I - \tilde{P}(T_l, \kappa_k, \gamma_k \Delta B_0) C(T_l, \tau_{1k}, \tau_{2k}) R(u_{1l}, u_{2l}) Q(u_{3l}, u_{4l}) \tilde{P}(T_l, \kappa_k, \gamma_k \Delta B_0) C(T_l, \tau_{1k}, \tau_{2k}),$

$\tilde{b}(u_l, t_k, \gamma_k \Delta B_0) =$

$\quad (\tilde{P}(T_l, \kappa_k, \gamma_k \Delta B_0) C(T_l, \tau_{1k}, \tau_{2k}) R(u_{1l}, u_{2l}) Q(u_{3l}, u_{4l}) + I) \tilde{P}(T_l, \kappa_k, \gamma_k \Delta B_0) D(T_l, \tau_{1k}).$

With these definitions, we can formulate the complete optimization

problem:

$$\max \quad \tilde{\lambda} \tag{3.2}$$
$$\text{s.t.} \quad \tilde{\lambda} \leq \lambda_{\Delta} \quad \forall \Delta B_0$$
$$S_{\Delta}^T S_{\Delta} - \lambda_{\Delta} I \succeq 0 \quad \forall \Delta B_0$$
$$\tilde{A}(u_l, t_k, \gamma_k \Delta B_0) \tilde{M}_{SS}(u_l, t_k, \gamma_k \Delta B_0) = \tilde{b}(u_l, t_k, \gamma_k \Delta B_0) \quad \forall l, k, \forall \Delta B_0$$
$$u_{1l}^2 + u_{2l}^2 \leq 1 \quad \forall l$$
$$u_{3l}^2 + u_{4l}^2 \leq 1 \quad \forall l$$
$$T_{\min} \leq T_l \leq T_{\max},$$

where $\Delta B_0 \in [\Delta B_{0,\min}, \Delta B_{0,\max}]$, and as in Section (2.3.2) $\gamma_k = \frac{\kappa_k}{B_0}$ depends only on tissue type. This is a semi-infinite optimization problem with nonlinear and semi-definite constraints. Although it is a theoretically interesting model, it is not practical to solve, since we have to maximize the minimum eigenvalue of the matrix $S_{\Delta}^T S_{\Delta}$ over all possible values of ΔB_0, which belongs to a set with infinite cardinality. Therefore, we need to consider discretization.

3.1.1 Discretized Problem

Discretization is a technique used to approximate the solution numerically. For example, in our case, if we take $J \in N$ discretization points, for the interval $[\Delta B_{\min}, \Delta B_{\max}]$ with each value (point) indexed by $j \in \{1, ..., J\}$, then the discretized model is as follows

$$\max \quad \tilde{\lambda} \tag{3.3}$$
$$\text{s.t.} \quad \tilde{\lambda} \leq \lambda_j \quad j \in \{1, ..., J\}$$
$$S_j^T S_j - \lambda_j I \succeq 0 \quad j \in \{1, ..., J\}$$
$$\tilde{A}(u_l, t_k, \gamma_k \Delta B_{0,j}) \tilde{M}_{SS}(u_l, t_k, \gamma_k \Delta B_{0,j}) = \tilde{b}(u_l, t_k, \gamma_k \Delta_j) \quad \forall j, l, k$$
$$u_{1l}^2 + u_{2l}^2 \leq 1 \quad \forall l$$
$$u_{3l}^2 + u_{4l}^2 \leq 1 \quad \forall l$$
$$T_{\min} \leq T_l \leq T_{\max}.$$

The number of discretization points is determined by the magnitude of field inhomogeneity, i.e., the fineness of the discretization needs to be tuned to the sensitivity of the objective with respect to ΔB_0 variation. The solution of the discretized, large-scale nonlinear semi-definite optimization problem needs

22
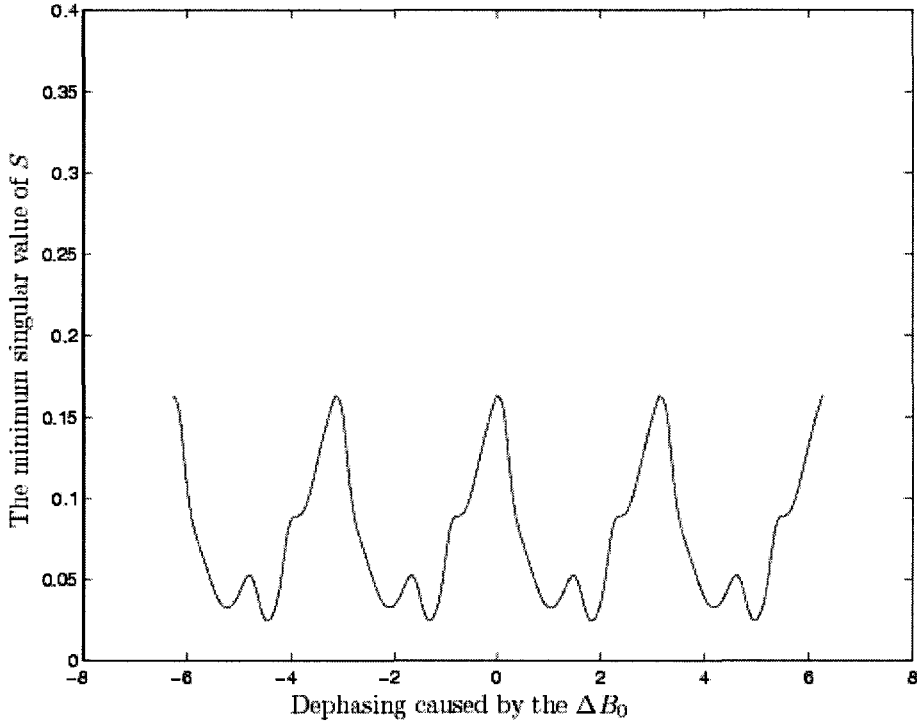
Figure 3.1: The fluctuation of the minimum singular value of S versus dephasing caused by the field inhomogeneity.

the development of dedicated algorithms. Due to time constraints, we did not explore this route, further, we found an easy-to-solve heuristic, which gave promising results.

3.2   Heuristic

An alternative way to handle the problem of field inhomogeneities is to exploit the properties of the matrices that are building blocks of the dynamical system. In this section, we explore the evolution of ΔB_0 and phase-cycling f. We demonstrate how off-resonance of the magnetization can be compensated by shifting phase-cycling. However, first we need to do some algebra to get an equivalent formulation of M_{SS} which makes the symmetry of P and Q

23

transparent.

We recall the formula (1.17) (see p.15.) that reflects the change of two consecutive states of the magnetization:

$$M_{k+1} = P\left(C\left(RQP\left(CM_k + D\right)\right) + D\right). \tag{3.4}$$

From (3.4) we note that at the kth time period, when M_k is flipped, it experiences a series of changes as rotation (R), RF pulse phase-cycling (Q), off-resonance (P) and relaxation (C), before the successive flip is carried out again, which results in off-resonance (P) and relaxation (C), causing the magnetization to achieve the magnetization M_{k+1}. Therefore, if we exert a phase-cycling Q after the second flip, which directly affects M_{k+1}, we expect this to be equivalent to the effect of only exerting a phase-cycling after the second time period other than the first time period, which can be formulated as:

$$\hat{M}_{k+1} = QP\left(C\left(RP\left(C\hat{M}_k + D\right)\right) + D\right). \tag{3.5}$$

Theorem 3.2.1. *Let the steady-state magnetization be achieved during the processes (3.4) and (3.5). Let M_{ss} and $\hat{M}_{ss}$ denote the steady-state magnetizations, respectively. Then the following relationship holds:*

$$\hat{M}_{ss} = QM_{ss}. \tag{3.6}$$

Proof. Writing (3.4) and (3.5) as steady-state forms, we have:

$$(I - PCRQPC)M_{ss} = PCRQPD + PD, \tag{3.7}$$
$$(I - QPCRPC)\hat{M}_{ss} = QPCRPD + QPD. \tag{3.8}$$

Since the rotations R, P, and Q have unit eigenvalues, and all the eigenvalues of the relaxation matrix C are less than one (and positive), $(I - PCRQPC)$ is invertible, so is $(I - QPCRPC)$ in (3.8). Therefore,

$$M_{ss} = (I - PCRQPC)^{-1}(PCRQPD + PD),$$

hence,

$$\begin{aligned} QM_{ss} &= Q(I - PCRQPC)^{-1}(PCRQPD + PD) \\ &= \left((I - PCRQPC)Q^{-1}\right)^{-1}(PCRQPD + PD) \end{aligned}$$

$$
\begin{aligned}
&= \left((I - PCRQPC)Q^{-1}\right)^{-1} Q^{-1} Q (PCRQPD + PD) \\
&= \left(Q\left((I - PCRQPC)Q^{-1}\right)\right)^{-1} (QPCRQPD + QPD) \\
&= \left(QIQ^{-1} - QPCRQPCQ^{-1}\right)^{-1} (QPCRQPD + QPD),
\end{aligned}
$$

since I is the identity matrix and commutes with any matrix, Q is orthogonal ($Q^{-1} = Q^T$), which commutes with C according to their structures, $QP = PQ$, and $QPD = PD = D$ (since D is a vector with the first and second component being zero, and the last rows and columns of P and Q are unit vectors, see (1.13), (1.14), and (1.16)), we have:

$$
\begin{aligned}
QM_{ss} &= \left(IQQ^{-1} - QPCRPQQ^{-1}C\right)^{-1} (QPCRQPD + QPD) \\
&= (I - QPCRPC)^{-1} (QPCRPD + QPD) \\
&= \hat{M}_{ss},
\end{aligned}
$$

based on (3.8).   □

We are only concerned with the x and y components of the steady-state M_{ss}, therefore:

$$
\begin{pmatrix} \cos(f) & \sin(f) \\ -\sin(f) & \cos(f) \end{pmatrix} \begin{pmatrix} M_{ss,x} \\ M_{ss,y} \end{pmatrix} = \begin{pmatrix} \hat{M}_{ss,x} \\ \hat{M}_{ss,y} \end{pmatrix}. \tag{3.9}
$$

For a three-experiment case in which $n = 3$ (see Section 2.2), we construct the matrix S based on (3.9) and obtain the relationship:

$$
US \;=\; \hat{S},
$$

in which,

$$
U = \begin{pmatrix}
\cos(f_1) & \sin(f_1) & 0 & 0 & 0 & 0 \\
-\sin(f_1) & \cos(f_1) & 0 & 0 & 0 & 0 \\
0 & 0 & \cos(f_2) & \sin(f_2) & 0 & 0 \\
0 & 0 & -\sin(f_2) & \cos(f_2) & 0 & 0 \\
0 & 0 & 0 & 0 & \cos(f_3) & \sin(f_3) \\
0 & 0 & 0 & 0 & -\sin(f_3) & \cos(f_3)
\end{pmatrix}, \tag{3.10}
$$

where the index of f corresponds to the experiment number.

25

Thus,

$$(\hat{S})^T \hat{S} = (US)^T(US) = S^T U^T U S = S^T S, \tag{3.11}$$

since U is an orthogonal matrix. Equality (3.11) implies that the steady-state matrices obtained from (3.4) and from (3.5) have the same singular values because their singular values are equal to the square root of the eigenvalues of $S^T S$ and $(\hat{S})^T \hat{S}$, respectively, which are equal. Therefore, we conclude that (3.4) is equivalent to (3.5) in terms of the usage in our optimization formulation.

3.2.1 Corrections for Field Inhomogeneity

We can write (3.8) by the decomposition $Q = \sqrt{Q} \cdot \sqrt{Q}$. Since $\sqrt{Q}$ has the same structure as Q, by comparing (3.7) and (3.8), we have:

$$(I - \sqrt{Q}PCR\sqrt{Q}PC)\hat{M}_{ss} = \sqrt{Q}PCR\sqrt{Q}PD + D \tag{3.12}$$

by a similar argument. If we take a closer look at equation (3.12), we observe that each appearance of P is preceded by a $\sqrt{Q}$. What is more interesting is that if we multiply $\sqrt{Q}$ and P, we have:

$$\sqrt{Q}P = \begin{pmatrix} \cos\left(\kappa T + \frac{f}{2}\right) & \sin\left(\kappa T + \frac{f}{2}\right) & 0 \\ -\sin\left(\kappa T + \frac{f}{2}\right) & \cos\left(\kappa T + \frac{f}{2}\right) & 0 \\ 0 & 0 & 1 \end{pmatrix}. \tag{3.13}$$

This tells us that the effect of magnetic field inhomogeneity could be compensated by adjustments to the RF pulse phase cycling as long as we have a map of the main magnetic field. Since P is transformed into $\tilde{P}$ in the presence of ΔB_0, we need to work with

$$\sqrt{Q}\tilde{P} = \begin{pmatrix} \cos\left(\kappa T + \gamma\Delta B_0 T + \frac{f}{2}\right) & \sin\left(\kappa T + \gamma\Delta B_0 T + \frac{f}{2}\right) & 0 \\ -\sin\left(\kappa T + \gamma\Delta B_0 T + \frac{f}{2}\right) & \cos\left(\kappa T + \gamma\Delta B_0 T + \frac{f}{2}\right) & 0 \\ 0 & 0 & 1 \end{pmatrix}. \tag{3.14}$$

In other words, we are able to handle nonuniform fields by **shifting** the RF pulse phase cycling correspondingly. This is illustrated by Figure 3.2, in

which we discretize uniformly as we did for ΔB_0 during the interval $[-4\pi, 4\pi]$ for the phase-cycling f. Comparing Figures 3.1 and 3.2, we can see that they manifest the same behavior. Of course, it is not practical (and possible) to do experiments with different shifting of RF pulse phase cycling for each pixel. In the next section we show that this individual shift of RF pulse phase cycling is not necessary.

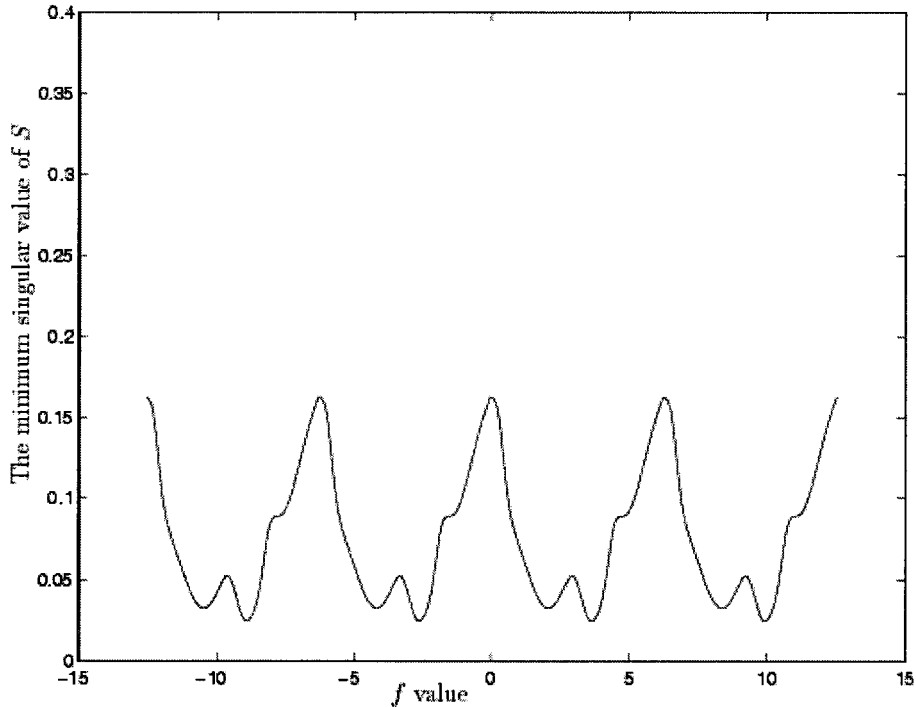Figure 3.2: The change of the minimum singular value of S corresponding to the shift of the RF pulse phase cycling.

3.2.2 Optimization Problem Based on the RF Pulse Phase Cycling Heuristic

Now we are able to formulate an optimization problem to make our SSFP pulse-sequence robust and insensitive to field inhomogeneity by employing a phase cycling shift heuristic. Without loss of generality, we only focus on one

period $[-\pi, \pi]$, since the response of the minimum singular value of the steady-state signal generation matrix to field inhomogeneity is periodic (see Figure 3.1). In our formulation, $\tilde{S}$ corresponds to the case where there is no shift of phase-cycling, and $\tilde{S}_{\xi_\zeta}$ corresponds to the shift of phase-cycling by the amount of ξ_ζ, in which ζ is the number of shifts. Assume 1000 points of discretization of field inhomogeneities, indexed by i, we have:

$$\max_{\xi_1, \xi_2, \ldots \xi_\zeta} \inf\{\lambda_i | i \in Y'\} \tag{3.15}$$

$$\text{s.t. } S_i^T S_i - \lambda_i I \succeq 0 \quad \forall i$$

$$S_i = (\tilde{S}_0, \tilde{S}_{\xi_1}, \tilde{S}_{\xi_2}, \cdots, \tilde{S}_{\xi_\zeta})^T$$

$$\tilde{A}(u_l, t_k, \gamma_k \Delta_i) \tilde{M}_{SS}(u_l, t_k, \gamma_k \Delta_i) = \tilde{b}(u_l, t_k, \gamma_k \Delta_i) \quad \forall l, k$$

$$\tilde{A}(u_l, t_k, \gamma_k \Delta_i + \frac{\xi_1}{T_l}) \tilde{M}_{SS}(u_l, t_k, \gamma_k \Delta_i + \frac{\xi_1}{T_l}) = \tilde{b}(u_l, t_k, \gamma_k \Delta_i + \frac{\xi_1}{T_l}) \, \forall l, k, i$$

$$\tilde{A}(u_l, t_k, \gamma_k \Delta_i + \frac{\xi_2}{T_l}) \tilde{M}_{SS}(u_l, t_k, \gamma_k \Delta_i + \frac{\xi_2}{T_l}) = \tilde{b}(u_l, t_k, \gamma_k \Delta_i + \frac{\xi_2}{T_l}) \, \forall l, k, i$$

$$\vdots$$

$$\tilde{A}(u_l, t_k, \gamma_k \Delta_i + \frac{\xi_\zeta}{T_l}) \tilde{M}_{SS}(u_l, t_k, \gamma_k \Delta_i + \frac{\xi_\zeta}{T_l}) = \tilde{b}(u_l, t_k, \gamma_k \Delta_i + \frac{\xi_\zeta}{T_l}) \, \forall l, k, i$$

$$u_{1l}^2 + u_{2l}^2 \leq 1 \quad \forall l$$

$$u_{3l}^2 + u_{4l}^2 \leq 1 \quad \forall l$$

$$\xi_{\zeta'} \in [-\frac{\pi}{2}, \frac{\pi}{2}] \, \forall \zeta'$$

in which $\tilde{S}_{\xi_\zeta}$ depends on $\tilde{M}_{SS}(u_l, t_k, \gamma_k \Delta_i + \frac{\xi_\zeta}{T_l})$ similarly to (NL-SDO).

Based on the equation (3.14) in which field inhomogeneity and phase cycling are linearly related, we can repeat the experiment multiple times with different shifts of phase cycling, so that all of the troughs from one curve (as shown in Figure 3.1) are covered by peaks from other curves, (see Figure 3.3). In other words, we solve the problem of low-quality tissue quantification by shifting the phase-cycling, in order to obtain good pulse-sequence design variables for better quantification. We realize this by multiple acquisitions of images and improve the images of inferior quality by averaging. We show the numerical results of repeating the experiment 15 times for each field inhomogeneity value, and calculate the minimum singular value (see Figure 3.4).

This model (3.15) is nonconvex and periodic, but it was easy to verify a good combination of ξ's based on the numerical experiments, as shown in
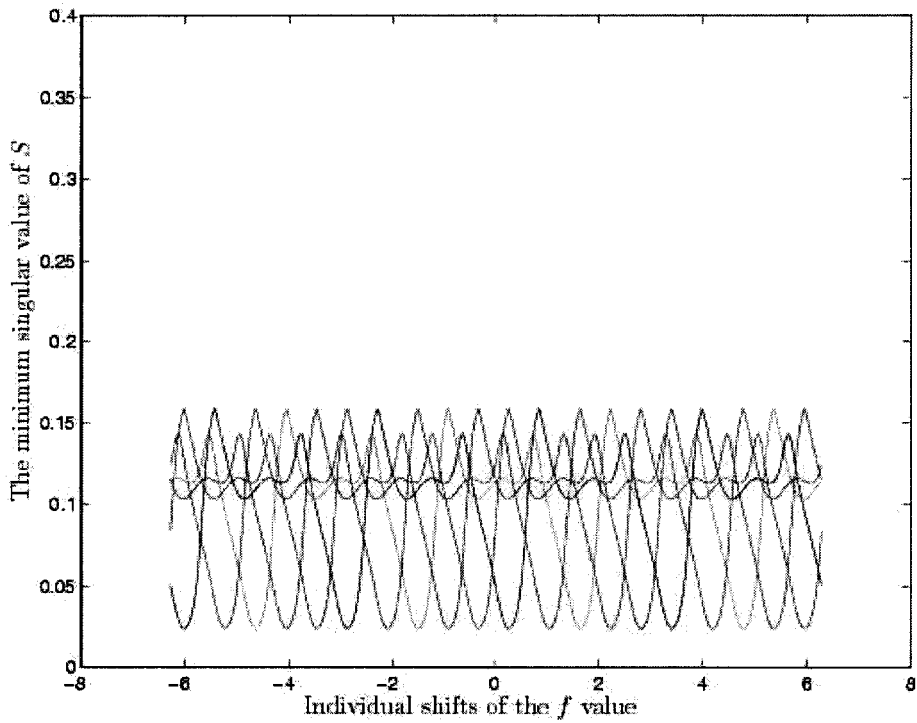
Figure 3.3: Multiple acquisition of images with different shifts

Figures (3.3) and (3.4).
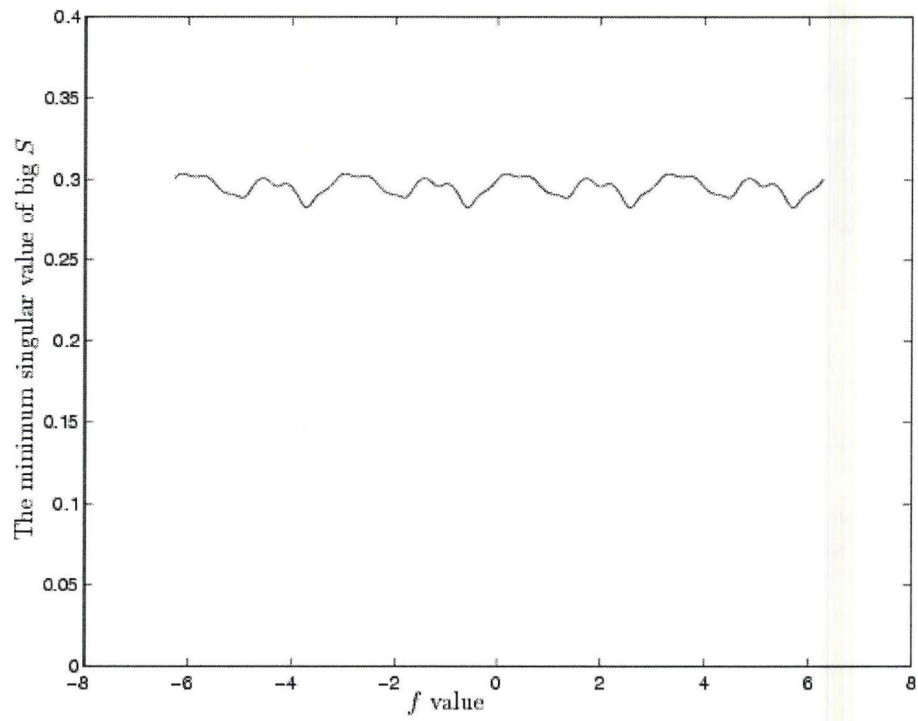
Figure 3.4: The minimum singular value versus B_0

Chapter 4

Total Variation Regularization Based Model

Tissue density estimation and field mapping can be cast as an inverse problem in which we would like to recover the original information about the image based on the available corrupted data. However, as is common in imaging, the problem is normally ill posed, which means that even for a small data perturbation, a large perturbation in the reconstruction can occur. To get around this, a regularization method is needed. The most common form of regularization is Tikhonov regularization [Tikhonov and Arsenin, 1977], in which a regularization parameter is set to regularize the output of the least squares solution. It has been used in a wide variety of applications, including image processing. While most of the regularization methods utilize prior knowledge and tend to smooth out the restored images, total variation preserves edges in the reconstructed image. Therefore, in this chapter, we first present the original total variation based model and then show how the model can be adapted to the MR imaging problem.

4.1   Total Variation Formulation

We are concerned with a bounded convex region $\Omega \subset \mathbb{R} \times \mathbb{R}$ in the 2-dimensional image plane. Let $\hat{u} : \Omega \to \mathbb{R}$, and $\hat{u}(x, y)$ be the observed intensity value of

the noisy image at location (x, y) in the region. Let $u : \Omega \to \mathbb{R}$, and $u(x, y)$ be the estimated intensity value of the original image at location (x, y) in the region; then

$$\hat{u}(x, y) = u(x, y) + \eta(x, y),$$

where $\eta : \Omega \to \mathbb{R}$, and $\eta(x, y)$ is an independently and uniformly distributed random variable representing the noise in the region. The gradient of a function is defined as a vector operator denoted by ∇. Let us suppose that σ is the standard deviation of the white noise, then the total variation based denoising model, proposed by Rudin et al. [Rudin et al., 1992], is as follows:

$$\min_{u} \int_{\Omega} |\nabla u| dx dy \tag{4.1}$$

$$\text{s.t.} \quad \|u - \hat{u}\|^2 = \sigma^2, \tag{4.2}$$

here $|\cdot|$ denotes the absolute value, and $\|\cdot\|$ denotes the l_2 norm. In the cases where the standard deviation of the noise σ is only imprecisely known, or known to have an upper bound, we relax the constraint (4.2) to $\|u - \hat{u}\|^2 \leq \sigma^2$. A number of algorithms have been suggested to solve the above problem in the literature, by solving the associated Euler-Lagrange equation of the minimization problem. Interested readers should refer to [Vogel and Oman, 1996].

In the meantime, Li and Santosa [Li and Santosa, 1996] considered a discretized version of the total variation model, in which, instead of a continuous image plane $\Omega = [0, a] \times [0, b]$, they focused on an array of pixels with $\check{m}$ columns and $\check{n}$ rows, and each pixel has width $a/\check{m}$ and height $b/\check{n}$. In other words, the image space is divided into $\check{n} \times \check{m}$ fine grids, and within each grid we assume that the intensity value is homogeneous. Therefore, the total variation of the image is approximated by

$$\mathrm{TV}^{(a)}(u) = \sum_{j=1}^{\check{m}} \sum_{i=1}^{\check{n}-1} \frac{b}{\check{n}} |u(i+1, j) - u(i, j)| +$$

$$\sum_{i=1}^{\check{n}} \sum_{j=1}^{\check{m}-1} \frac{a}{\check{m}} |u(i, j+1) - u(i, j)|. \tag{4.3}$$

The discretized formulation bases the total variation of the image on the difference of the individual pixels, which is suitable for the pixel-wise operation in the MRI. In other words, the total variation of the image can be interpreted as the summation of the vertical and horizontal variations of every

single pixel (see Figure 4.1(a)). Note that (4.3) is the l_1 norm of a vector in the $\breve{m}(\breve{n}-1)+\breve{n}(\breve{m}-1)$ dimensional space, and it is not differentiable whenever a component is zero. To make it smooth, we reformulate by switching to the sum of l_2 norms and by introducing a small positive constant $\varrho \in \mathbb{R}_+$:

$$
\mathrm{TV}_\varrho^{(a)}(u) = \sum_{j=1}^{\breve{m}} \sum_{i=1}^{\breve{n}-1} \frac{b}{\breve{n}} \sqrt{(u(i+1,j)-u(i,j))^2 + \varrho} +
$$
$$
\sum_{i=1}^{\breve{n}} \sum_{j=1}^{\breve{m}-1} \frac{a}{\breve{m}} \sqrt{(u(i,j+1)-u(i,j))^2 + \varrho}. \tag{4.4}
$$

Alternatively, (4.3) can be slightly modified into the following form (see Figure 4.1(b)):

$$
\mathrm{TV}_\varrho^{(b)}(u) =
$$
$$
\sum_{i=1}^{\breve{n}-1} \sum_{j=1}^{\breve{m}-1} \sqrt{(\frac{b}{\breve{n}}(u(i+1,j)-u(i,j)))^2 + (\frac{a}{\breve{m}}(u(i,j+1)-u(i,j)))^2 + \varrho}. \tag{4.5}
$$

We can visualize the differences between the two above measures, as in Figure 4.2. We notice that the unit ball on the right is rotationally invariant, whereas the one on the left is directionally dependent. In addition, since a pixel is correlated with all its neighbor pixels, we expect that the variation of a pixel could be modelled in many ways other than vertically and horizontally. For example, we can present another scheme that is based on the variations of diagonal pixels (see Figure 4.1(c)):

$$
\mathrm{TV}_\varrho^{(c)}(u) =
$$
$$
\sum_{j=1}^{\breve{m}-1} \sum_{i=1}^{\breve{n}-1} \sqrt{(\frac{b}{\breve{n}}(u(i+1,j+1)-u(i,j)))^2 + (\frac{a}{\breve{m}}(u(i+1,j)-u(i,j+1)))^2 + \varrho}. \tag{4.6}
$$

We would like to point out that even though there are other ways to formulate total variation, we do not list all of them here. The three different ways of formulating the total variation have distinct computational cost, for which we will give a detailed analysis in Section 4.4.
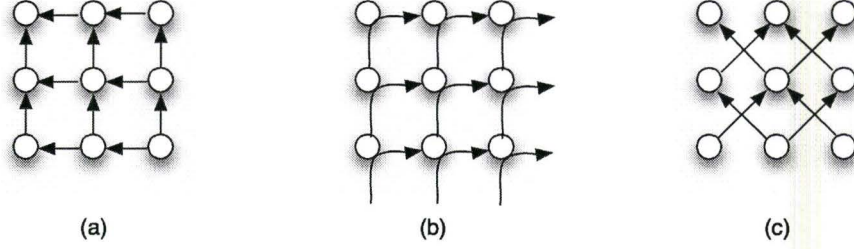
Figure 4.1: Graphical representation of total variation function based on three different schemes. The pixels that each arrow traverses represent those that a specific term in the total variation depends on.

4.2 Mathematical Model

Now we will show how to use total variation to regularize the estimation of tissue densities in the context of MRI. To reconstruct the image, we measure the projection of the magnetization onto the plane perpendicular to the external magnetic field as a complex-valued signal. Suppose that we are dealing with three different tissue types defined on the same region Ω, $\rho_1 : \Omega \rightarrow \mathbb{R}$, $\rho_2 : \Omega \rightarrow \mathbb{R}$, $\rho_3 : \Omega \rightarrow \mathbb{R}$ respectively. The field inhomogeneity strength at each pixel is defined as $\Delta B_0 : \Omega \rightarrow \mathbb{R}$. The observed signal generated from the MR machine is defined as $s_0 : \Omega \rightarrow \mathbb{R}^2$. In order to formulate the total variation based tissue density estimation model, we let $\rho_t(i,j) \in \mathbb{R} : t \in \{1,2,3\}, 1 \leq i \leq \check{n}, 1 \leq j \leq \check{m}$ be the estimated intensity value of the tissue type t at the pixel (i,j), and we define a vector $\rho \in \mathbb{R}^{3\check{m}\check{n}}$ as

$$
\begin{aligned}
\rho = \ & (\rho_1(1,1), \rho_2(1,1), \rho_3(1,1), ..., \rho_1(1,\check{m}), \rho_2(1,\check{m}), \rho_3(1,\check{m}), \\
& \rho_1(2,1), \rho_2(2,1), \rho_3(2,1), ..., \rho_1(2,\check{m}), \rho_2(2,\check{m}), \rho_3(2,\check{m}), \\
& ..., \rho_1(\check{n},\check{m}), \rho_2(\check{n},\check{m}), \rho_3(\check{n},\check{m}))^T.
\end{aligned}
$$

Let $\Delta B_0(i,j) \in \mathbb{R}$ be the field inhomogeneity magnitude at the pixel (i,j), and we define the vector $\Delta \bar{B}_0 \in \mathbb{R}^{\check{m}\check{n}}$

$$
\Delta \bar{B}_0 = (\Delta B_0(1,1), ..., \Delta B_0(1,\check{m}), ..., \Delta B_0(\check{n},1), ..., \Delta B_0(\check{n},\check{m}))^T.
$$

Steady-state magnetization of tissue type t at a point (i,j) depends on $\Delta B_0(i,j)$, which is define as $M_{SS}^t : \mathbb{R}^2 \rightarrow \mathbb{R}^3, t \in (1,2,3)$, the 3-dimensional magnetization of the tissue type t under an experiment. Let $\bar{s}(i,j) \in \mathbb{R}^2$ be the observed

$$\sqrt{x^2 + 0.01} + \sqrt{y^2 + 0.01} - 1 = 0 \qquad \sqrt{x^2 + y^2 + 0.01} - 1 = 0$$
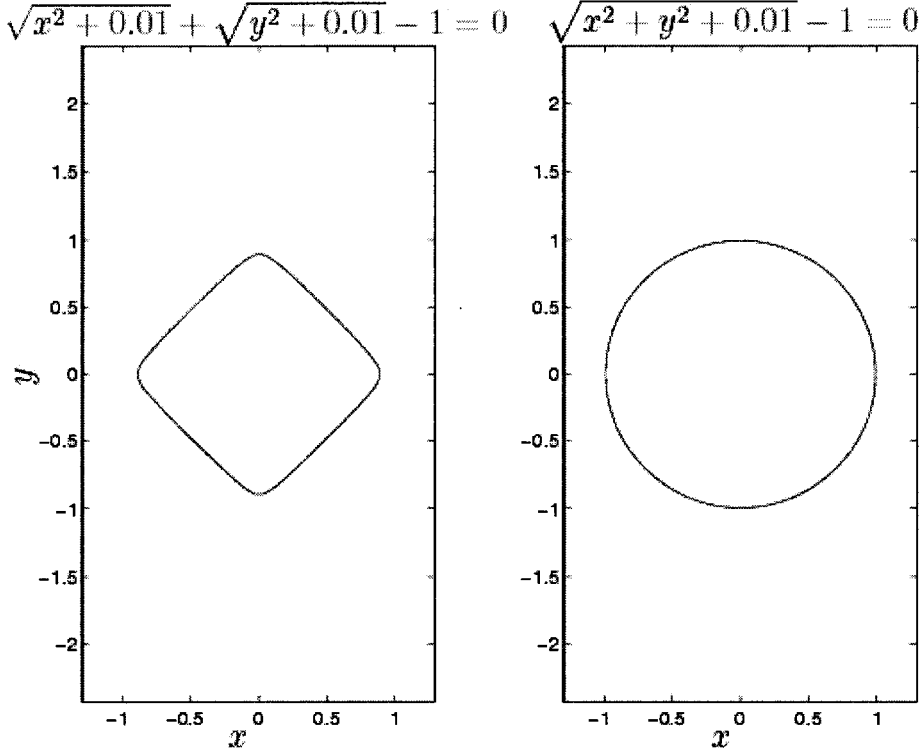
Figure 4.2: The pictures of unit balls for two different formulations with constant $\varrho = 0.01$, corresponding to (a) and (b) of Figure 4.1, respectively.

signal strength at pixel (i, j), and we define

$$\bar{s} = (s_{0,x}(1,1), s_{0,y}(1,1), s_{0,x}(1,2), s_{0,y}(1,2), ..., s_{0,x}(\breve{n}, \breve{m}), s_{0,y}(\breve{n}, \breve{m})) \in \mathbb{R}^{2\breve{m}\breve{n}}.$$

In addition, we define a block diagonal transformation matrix $\tilde{S} \in \mathbb{R}^{2\breve{m}\breve{n} \times 3\breve{m}\breve{n}}$ that has 2×3 blocks at positions from $(2i - 1, 3j - 2)$ to $(2i, 3j)$,

$$\text{Block}_{i,j} = \begin{bmatrix} M_{1,x}(\Delta B_0(i,j)) & M_{2,x}(\Delta B_0(i,j)) & M_{3,x}(\Delta B_0(i,j)) \\ M_{1,y}(\Delta B_0(i,j)) & M_{2,y}(\Delta B_0(i,j)) & M_{3,y}(\Delta B_0(i,j)) \end{bmatrix}$$

$$\tilde{S} = \begin{bmatrix} \text{Block}_{i,j} & & & & \\ & \ddots & & & \\ & & \text{Block}_{1,\breve{m}} & & \\ & & & \text{Block}_{2,1} & \\ & & & & \ddots & \\ & & & & & \text{Block}_{\breve{n},\breve{m}} \end{bmatrix}, \qquad (4.7)$$

or, $\tilde{S} = \text{blockdiag}(\text{Block}_{i,j}|i = 1, ..., \breve{n}, j = 1, ..., \breve{m})$, with each block corresponding to a single pixel in the image. Now we propose a total variation regularization formulation that takes into account both the total variation of tissue densities and field inhomogeneity, as well as the similarity of the estimated signal to the measurements.

$$
\min_{\rho, \Delta \bar{B}_0} \quad \|\tilde{S}\rho - \bar{s}\|^2 + \lambda_1 \text{TV}(\rho_1) + \lambda_2 \text{TV}(\rho_2) + \lambda_3 \text{TV}(\rho_3) + \lambda_4 \text{TV}(\Delta B_0)
$$
$$
\text{s.t.} \quad \rho \geq 0 \tag{TV}
$$

where $\lambda_1, \lambda_2, \lambda_3, \lambda_4$ are regularization parameters, and TV represents the total variation (see (4.4)). We can also reformulate the above as a barrier function, in the following function:

$$
\begin{aligned}
\upsilon(\Delta \bar{B}_0, \rho, \mu) = \quad & \|\tilde{S}\rho - \bar{s}\|^2 + \lambda_1 \text{TV}(\rho_1) + \lambda_2 \text{TV}(\rho_2) + \lambda_3 \text{TV}(\rho_3) + \lambda_4 \text{TV}(\Delta B_0) \\
& -\mu \Big(\sum_{i=1}^{\breve{n}} \sum_{j=1}^{\breve{m}} (\log(\rho_1(i,j)) + \log(\rho_2(i,j)) + \log(\rho_3(i,j))) \Big), \quad (4.8)
\end{aligned}
$$

in which μ is the barrier parameter. We can solve this problem by solving a sequence of unconstrained minimization problems of the form $\min_{\Delta \bar{B}_0, \rho} \upsilon(\Delta \bar{B}_0, \rho, \mu)$ for a sequence of μ that decrease monotonically to zero. The optimal solution depends on the selection of the regularization parameters that yields a regularized output.

4.3 Notes about Regularization Parameters

The purpose of imposing regularization is that the solutions given by the least squares $\|\tilde{S}\rho - \bar{s}\|^2$ may be dominated by contributions from data errors and rounding errors. However, we expect to reduce the negative contributions while keeping the regularization at a reasonable size by selecting proper regularization parameters. In other words, we need to trade off between the fit to the given data and the variation in the regularized solution in a way that a reasonable balance is achieved. In addition, it is necessary to assign different regularization parameters to the different tissues and field inhomogeneity since they are independent quantities in our case. In addition, the decision also bears a certain clinical relevance. For example, many brain diseases are associated with patterns of atrophy that may be distinctive in the distribution of different

tissues [Coffey et al., 1992]. Therefore, volumetric data describing the distribution of brain tissue types, such as cerebrospinal fluid (CSF), white matter (WM), grey matter (GM) have been widely used in studies of normal aging and disease process. CSF is a clear, colorless liquid that circulates around and within the central nervous system occupying cavities within the brain and the subarachnoid space around it. The WM, together with the GM also called the cortex, comprise the core of the cerebellum that coordinates our motor activity, posture, and balance. The curves of variation for the three different tissue types are distinct [Haacke et al., 1999], so a different regularization is desired. To gain a sense of the general case, please refer to the book by P.C. Hansen [P.C. Hansen, 2001]. In this thesis, we did not explore the optimal selection (combination) of the regularization parameters, because we believe that it is computationally demanding to conduct a brute force search for the parameters with a variable size in our problem involved, unless we find a better way to approach the problem of selecting the regularization parameters.

4.4   Sparsity Pattern and Complexity Analysis

Now we would like to explore the sparsity pattern of the function (4.8). If we apply Newton's method to solve it, we need to calculate the gradient as well as the Hessian of the function (4.8) in order to find out the Newton search direction, i.e., at least we need to store a vector size of $4\breve{m}\breve{n}$ for the gradient, and a matrix size of $4\breve{m}\breve{n} \times 4\breve{m}\breve{n}$ for the Hessian. For example, for a typical image size of 256×256, the Hessian matrix would be of size $16 \times 256^4 \simeq 1.6 \times 10^{11}$! Therefore, computing the search direction seems to be computationally challenging for Newton's method in this case. However, the Hessian matrix is very sparse. We will justify our statement by analyzing the sparsity pattern now.

For a different set of regularization parameters, (4.8) comes as a different optimization problem, and for each iteration in solving the problem, the barrier parameter μ is fixed. Therefore, we have the variable size for each iteration as follows:

$$(\rho_1(1,1), \cdots, \cdots, \rho_1(\breve{n}, \breve{m}),$$
$$\rho_2(1,1), \cdots, \cdots, \rho_2(\breve{n}, \breve{m}),$$
$$\rho_3(1,1), \cdots, \cdots, \rho_3(\breve{n}, \breve{m}),$$

$$\Delta B_0(1,1), \cdots, \cdots, \Delta B_0(\check{n}, \check{m})),$$

namely, $3\check{m}\check{n} + \check{m}\check{n} = 4\check{m}\check{n}$ variables.

For the formulation (4.4), we calculate the first element of the gradient and find out that $\frac{\partial v}{\partial \rho_1(1,1)}$ depends on

$$(\rho_1(1,1), \rho_2(1,1), \rho_3(1,1), \Delta B_0(1,1), \rho_1(1,2), \rho_1(2,1)),$$

i.e., a function of only 6 variables. So if we take the Hessian, the first row of which would consist of $4\check{m}\check{n}$ elements obtained by taking the derivative of the above function with respect to all variables. Thus, it is easy to see that there are only 6 nonzero entries in the first row, with all others being zeros. Based on the observation of the structure of the v function, we would be able to generalize the results that for the $3\check{m}\check{n}$ variables in the form of $\rho_t(i,j)$, $\frac{\partial v}{\partial \rho_t(i,j)}$ contains at most eight variables, should they all exist:

$$(\rho_1(i,j), \rho_2(i,j), \rho_3(i,j), \Delta B_0(i,j),$$
$$\rho_t(i-1,j), \rho_t(i+1,j), \rho_t(i,j-1), \rho_t(i,j+1)),$$

which means that for the first $3\check{m}\check{n}$ rows altogether, the Hessian matrix contains at most $3\check{m}\check{n} \times 8 = 24\check{m}\check{n}$ nonzeros.

For the variables in the form of $\Delta B_0(i,j)$, $\frac{\partial v}{\partial \Delta B_0(i,j)}$ contains at most eight variables, should they all exist:

$$(\rho_1(i,j), \rho_2(i,j), \rho_3(i,j), \Delta B_0(i,j), \Delta B_0(i-1,j),$$
$$\Delta B_0(i+1,j), \Delta B_0(i,j-1), \Delta B_0(i,j+1)),$$

which means that for the last $\check{m}\check{n}$ rows, the Hessian matrix contains at most $\check{m}\check{n} \times 8$ nonzeros. Therefore, the Hessian matrix has at most $24\check{m}\check{n} + 8\check{m}\check{n} = 32\check{m}\check{n}$ nonzero entries. In fact, the bound is not tight and the Hessian should be even sparser, considering the fact that at the boundary, each pixel has only two or three adjacent pixels (depending on whether that pixel is at the corner or not) instead of four.

With similar analysis, we may calculate the number of nonzero entries for formulation (4.5). For the variables in that form of $\rho_t(i,j)$, $\frac{\partial v}{\partial \rho_t(i,j)}$ contains at most nine variables, should they all exist:

$$(\rho_1(i,j), \rho_2(i,j), \rho_3(i,j), \Delta B_0(i,j), \rho_t(i-1,j), \rho_t(i+1,j),$$

$$\rho_t(i, j-1), \rho_t(i, j+1), \rho_t(i+1, j-1)),$$

and for the variables in that form of $\Delta B_0(i,j)$, $\frac{\partial v}{\partial \Delta B_0(i,j)}$ depends on at most nine variables, namely:

$$(\rho_1(i,j), \rho_2(i,j), \rho_3(i,j), \Delta B_0(i,j), \Delta B_0(i-1,j),$$
$$\Delta B_0(i+1,j), \Delta B_0(i,j-1), \Delta B_0(i,j+1), \Delta B_0(i+1,j-1)).$$

Note that the gradient now depends on more variables, we expect to end up with a denser Hessian matrix. Indeed the Hessian matrix contains at most $36\breve{m}\breve{n}$ nonzero entries.

For the formulation (4.6), any pixel is correlated with all its adjacent pixels, thus for the variables in that form of $\rho_t(i,j)$, $\frac{\partial v}{\partial \rho_t(i,j)}$ contains at most twelve variables, should they all exist:

$$(\rho_1(i,j), \rho_2(i,j), \rho_3(i,j), \Delta B_0(i,j), \rho_t(i-1,j), \rho_t(i+1,j), \rho_t(i,j-1),$$
$$\rho_t(i,j+1), \rho_t(i+1,j+1), \rho_t(i-1,j-1), \rho_t(i+1,j-1), \rho_t(i-1,j+1)),$$

and for the variables in that form of $\Delta B_0(i,j)$, $\frac{\partial v}{\partial \Delta B_0(i,j)}$ depends on at most twelve variables:

$$(\rho_1(i,j), \rho_2(i,j), \rho_3(i,j), \Delta B_0(i,j), \Delta B_0(i-1,j),$$
$$\Delta B_0(i+1,j), \Delta B_0(i,j-1), \Delta B_0(i,j+1), \Delta B_0(i+1,j+1),$$
$$\Delta B_0(i-1,j-1), \Delta B_0(i+1,j-1), \Delta B_0(i-1,j+1),).$$

Therefore, the Hessian contains at most $48\breve{m}\breve{n}$ nonzero entries.

We also note that the sparsity pattern of the Hessian matrix varies with the ordering of the variables. If the variables are organized in the pixel-clustered manner, i.e., in the form of

$$\rho_1(1,1), \rho_2(1,1), \rho_3(1,1), \Delta B_0(1,1), \cdots,$$
$$\rho_1(\breve{n}, \breve{m}), \rho_2(\breve{n}, \breve{m}), \rho_3(\breve{n}, \breve{m}), \Delta B_0(\breve{n}, \breve{m}),$$

then the Hessian matrix exhibits an interesting sparsity pattern as shown in Figure 4.3 for all the three TV models. However, if we organize the variables in a sequential manner as follows:

$$\rho_1(1,1), \cdots, \rho_1(\breve{n}, \breve{m}),$$
$$\rho_2(1,1), \cdots, \rho_2(\breve{n}, \breve{m}),$$

39

$$\rho_3(1,1), \cdots, \rho_3(\check{n},\check{m}),$$
$$\Delta B_0(1,1), \cdots, \Delta B_0(\check{n},\check{m}),$$

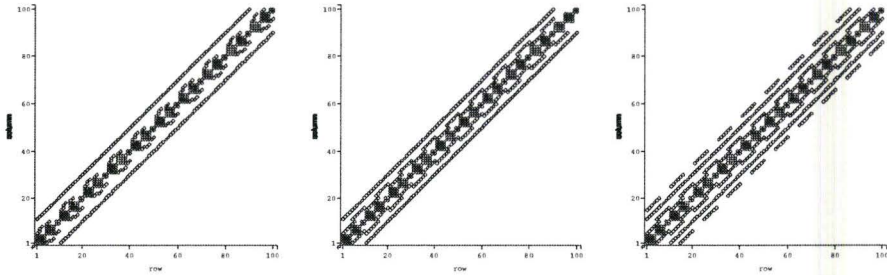then the Hessian matrix becomes an even sparser banded matrix as shown in Figure 4.4.

Figure 4.3: The sparsity pattern corresponding to the formulation (4.4),(4.5), and (4.6) respectively, with variables organized in a pixel-clustered manner.
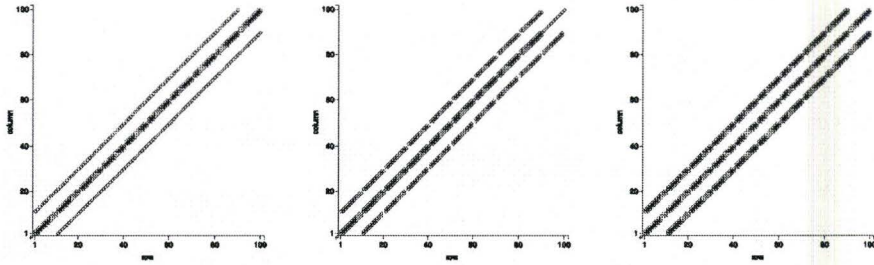

Figure 4.4: The sparsity pattern corresponding to the formulation (4.4),(4.5), and (4.6) respectively, with variables organized in a sequential manner.

4.5 Tissue Quantification and Field inhomogeneity Estimation with Total Variation Regularization

In this section, we will show how to use total variation regularized model (see (TV)) to estimate tissue density and field inhomogeneity, by decomposing the original problem into two interleaved subproblems that can be solved by a coordinate search in a lower dimension subspace. More specifically, we would like to estimate the field inhomogeneity ΔB_0 as a first subproblem, then we continue to solve the tissue density estimation subproblem by fixing ΔB_0 as estimated. By solving the two subproblems, we are able to obtain both field inhomogeneity and tissue density estimates.

4.5.1 The First Subproblem: Field Inhomogeneity Estimation

The model for estimating the ΔB_0 is as follows:

$$\min \quad \|\tilde{S}(\tilde{S}^T\tilde{S})^{-1}\tilde{S}^T\bar{s} - \bar{s}\|^2 + \lambda \text{TV}(\Delta B_0), \tag{4.9}$$

in which $\tilde{S}$ (see equation (4.7)) depends on ΔB_0 at each pixel. We attempt to estimate ΔB_0 without knowing tissue density by minimizing a residual between the estimated signal and the simulated signal (in our case) with total variation regularization, because we expect that the estimated ΔB_0 would be such that the signal generated with this ΔB_0 is as close to the simulated signal as possible while the smooth property of the field inhomogeneity is still preserved. Without loss of generality, we assume that the field variation falls into a specific range. This is reasonable since the tissue variability is known, and main magnets have manufacturing tolerances. The range is determined in accordance with the ΔB_0 data simulated, i.e., our purpose is to estimate precisely the simulated ΔB_0 from our model based on this range. In the real experiment, we will derive ΔB_0 from the image data. But in order to validate the algorithm, we need to simulate data with known ΔB_0 values.

41

4.5.2   The Second Subproblem: Tissue Density Estimation

Next, we would like to estimate the tissue densities based on the information obtained from estimating the field inhomogeneity. The subproblem for estimating the tissue density is as follows:

$$\min_{\rho^*} \quad f = \|\tilde{S}\rho^* - \bar{s}\|^2 + \lambda_1 \mathrm{TV}(\rho_1) + \lambda_2 \mathrm{TV}(\rho_2) + \lambda_3 \mathrm{TV}(\rho_3), \qquad (4.10)$$

Since we want to harness the field inhomogeneity estimate, we would assume that the ΔB_0 term is already known. In our experiment, $\rho^* = [\rho_1, \rho_2, \rho_3]^T$ represents the concatenation of the three different tissue types, namely:

$$\rho_1 = (\rho_1(1,1), \rho_1(1,2), \cdots, \rho_1(2,1), \rho_1(2,2), \cdots, \cdots, \rho_1(15,15))$$
$$\rho_2 = (\rho_2(1,1), \rho_2(1,2), \cdots, \rho_2(2,1), \rho_2(2,2), \cdots, \cdots, \rho_2(15,15))$$
$$\rho_3 = (\rho_3(1,1), \rho_3(1,2), \cdots, \rho_3(2,1), \rho_3(2,2), \cdots, \cdots, \rho_3(15,15)).$$

For the 15×15 image with three different tissue types that we simulated, there are $3 \times 15 \times 15$ variables involved. This variable size is much bigger than that of the model for field inhomogeneity estimation.

Chapter 5

Results and Numerical Simulation

In this chapter, we present the results of our algorithms and numerical simulation in two parts. The first part contains a brief description of our sequential, semi-definite, trust-region method used to solve the semi-definite optimization problem (NL-SDO), followed by a numerical simulation that demonstrates an application of our method in carotid artery tissue quantification. The second part consists of numerical results for field inhomogeneity as well as tissue density estimation based on our total variation regularized model.

5.1   Tissue Quantification with Homogeneous Field

We solve the nonlinear semi-definite problem (NL-SDO) by solving a sequence of linear mixed semi-definite (SDO) and second order cone (SOCO) trust region subproblems. We chose to fix the values of T_l in the nonlinear problem because T_l appear in multiple places in the constraints, and we couldn't find a suitable change of coordinates to reduce the nonlinearity. We use the optimization software SeDuMi [Sturm, 1999] to solve the subproblems. For detailed description of our algorithm and numerical results, please refer to Appendix A.

43

5.1.1 Numerical Phantom (Carotid Artery)

In this section we demonstrate the applicability of our method by numerically simulating carotid artery tissue quantification. Intraluminal lipids, *i.e.*, fat deposits inside arteries, are an indication of arterial disease. For example, some strokes are caused by the rupturing of large lipid deposits in the carotid artery, which carries blood from the heart to the brain. Figure 5.1 depicts a cross section of an idealized carotid artery containing intraluminal lipid. Large arteries are essentially composed of a tube of muscle (which contracts in sympathy with the heart to increase blood flow), containing (flowing) blood and surrounded by fat (and other) tissues. For simplicity, we ignore the surrounding tissue which is not fat. In Figure 5.1, we also show a layer of lipid deposited uniformly on the inside of the vessel wall. The exact distribution of lipids is not important, since we have not chosen a resolution sufficient to determine the exact distribution.

Numerical Results for Tissue Quantification

Table 5.1 shows the relative performance of optimal pulse sequence designs using our method for the cases of 3, 4, and 6 experiments. In all cases, we use the sum of the fat components of all of the voxels marked with a Σ in Figure 5.1 to estimate the total intraluminal lipids in this cross section. The estimated intraluminal lipid is close to the actual value in the simulations, for all numbers of experiments, but more importantly, the standard deviation of the lipid quantification decreases as a function of the number of experiments, and it does so faster than one would obtain by simply averaging the three experiments to reduce noise in the source images. The standard deviations in the simulation are also consistent with the deviations predicted by the objective function.

Comparison with MR Spectroscopy

Superimposed on the vessel structure is a $1mm$ grid representing the voxel size for SSFP tissue quantification, whereas the entire figure represents a single voxel for MR spectroscopy. The SSFP pulse-sequence has higher spatial resolution than MR spectroscopy, and no matter how we line up this $1cm^2$

44

	3-Ex	4-Ex	6-Ex	Zero-noise
Actual intraluminal lipid	5.4000	5.4000	5.4000	5.4000
Estimated intraluminal lipid	5.4028	5.4016	5.3987	5.4000
Standard deviation of the est.	0.0735	0.0650	0.0467	0.0000
Expected std. deviation from ave.	0.0735	0.0637	0.0520	0.0000
Expected std. deviation from obj.	0.0735	0.0610	0.0497	0.0000

Table 5.1: Numerical results for tissue density estimation based on 1000 experiments, measured in mm^2.

voxel, we cannot separate the intraluminal lipids from the extraluminal lipids. Furthermore, a spectroscopic examination would take on the order of minutes, whereas the individual SSFP images at this resolution would only require $256 \times 6ms$, or about 1.5 seconds.

Comparison with Dixon Method

In order to demonstrate the advantage of generalizing the Dixon method by allowing arbitrary phase relationships between tissues (as expressed in the S matrix), we compare a 3 tissue-experiment with pulse sequence design variables optimized according to the model (see (NL-SDO)) with a 3-experiment result using conventional phase relationships:

$$S^{\mathbb{C}} = \begin{pmatrix} 1 & 1 & 1 \\ 1 & -1 & 1 \\ 1 & -1 & -1 \end{pmatrix}. \tag{5.1}$$

To be comparable, we use SSFP sequences for the conventional Dixon case, with pulse-sequence design variables in the same ranges. We used a grid-search to find design values which result in an $S^{\mathbb{C}}$ of the form (5.1), after an overall complex scaling, and we allow a variation of 5 per cent in each entry. We allowed the variation in each entry to make the grid search reasonable. To not disadvantage the conventional case, we also use the Moore-Penrose Pseudo-Inverse for this case. The resulting three sets of pulse-sequence design variables are listed in Table 5.2.

The advantage of optimal sequence design over the design based on the conventional Dixon phase relationships is clear in a numerical simulation of the carotid artery simulation described by Figure 5.1. Figure 5.2 shows gray-

45

α	f	T
4.0	45.0	1.2
1.0	21.0	4.9
1.0	86.5	5.0

Table 5.2: Pulse-sequence design variables for Dixon method, where α and f are in degrees and T is in ms.

scale images reconstructed by applying the Moore-Penrose Pseudo-Inverse to simulated SSFP images, for different sequence designs, but with identical noise, to render noise effects comparable. The final row shows the results of the conventional Dixon phase relationships. The middle rows are the result of our algorithm, using only the grid search, and the grid search followed by the iterative method. The first row is the ideal case with zero noise. Note that without noise, all reconstruction methods and sequence designs produce the same results.

5.2 Tissue Quantification with Total Variation Regularization in the Presence of Field Inhomogeneity

5.2.1 The First Subproblem

Simulation of Field Inhomogeneity

The field inhomogeneity is caused by machine imperfections and tissue susceptibility of the object being imaged,

$$\Delta B_0 = \Delta B_{0(\text{magnet})} + \Delta B_{0(\text{tissue})}.$$

The main magnetic field inhomogeneity $\Delta B_{0(\text{magnet})}$ is a slowly varying function in space, thereby approximately constant within a small region. By contrast, the susceptibility field inhomogeneity is rapidly varying, since the value of the gyromagnetic constant induces a frequency shift even for a few parts per million (ppm) static field variation, which in turn leads to significant distortions in image geometry and intensity. In the case of tissues with different

46

susceptibility, we expect a strong field variation across the interface of two tissues.

Numerically, we simulate both parts of the field inhomogeneity as discussed above. The contribution from the magnet can be considered random, since we have no control over the location of the imperfections. Hence, we approximate the field inhomogeneity from the magnet by a random polynomial in our experiment. On the other hand, since different tissue types with different susceptibility values exhibit distinct local field variations, and those values are empirically determined and (for some tissues) available in the literature, we would be able to obtain the local field variation for each tissue type. Because the field map is the restriction of a solution of Maxwell's equation [Zwillinger, 1997], it is smooth. Therefore, we smooth the ΔB_0 component from the tissue susceptibility using 2-D Gaussian smoothing, which is a point-spread function with standard deviation σ_0:

$$G(x, y) = \frac{1}{2\pi\sigma_0^2} e^{-\frac{x^2+y^2}{2\sigma_0^2}} .$$

In our experiment, the simulated ΔB_0 from the main magnet and from the tissue susceptibility are shown in Figure 5.3.

Simulation of Collected Signal

The ΔB_0 data is necessary for simulating the signal that would be produced by the MR machine, which is represented by $\bar{s}$ in our model. As explained earlier, our signal generation is measured on an individual pixel basis, which means that the signal emanating from each pixel depends only on tissue density distribution and field inhomogeneity at that pixel. Since we have simulated ΔB_0 information for each pixel, we are able to simulate the signal $\bar{s}$ for the whole image. The simulated signal of the 15×15 image, viewed as a 225 pixel vector is shown in Figure 5.4:

Grid Search

Since (4.9) is not convex with respect to the ΔB_0 (after examining the structure of $\tilde{S}$), it is possible that a local search algorithm (such as Newton's method)

converges to a local minimum other than the desired global one. Therefore, the choice of starting point is very important. We choose a starting point using pixel-wise grid search in ΔB_0 for the least residual (the least squares part of (4.9)). In our experiment, we discretize the possible range of ΔB_0 into 1000 equally spaced points for each pixel and search for the best one that yields the least residual between the generated signal and the simulated signal. We choose 1000-grid based on the fineness of the ΔB_0 simulation. We expect to cover all the data by taking the discretization of this precision. We believe that this is necessary for the accuracy of the starting point by performing a grid search with the 1000 points. Suppose that the simulated ΔB_0 is within the range $[-0.1, 0.7]$, then we perform the grid search for a specific pixel for 1000 times, see Figure 5.5. However, based on the computational consideration, we can also discretize the range up to some specified precision that would lead to a sparser grid. If the discrepancy is small, this would not undermine the accuracy while saving computation time, which is demonstrated in Figure 5.6. For an image of size 15×15, the grid search corresponding to 1000 and 500 points means $15 \times 15 \times 1000$ times and $15 \times 15 \times 500$ times of computation, respectively. Since the contrived signal is close to the simulated signal up to added noise, we expect that the estimate ΔB_0 and the real ΔB_0 are close to each other as well. Taking the solution from the grid search as a starting point, the local minimum to which the local search algorithm converges is also a global minimum, since the starting point is already very close to the real solution. We have tested this idea numerically and found out that it works, see Figure 5.7.

However, even though this approach has many advantages, it is too expensive. For an image of typical size 256×256, it would be time consuming to perform the grid search for all pixels, since it requires $256 \times 256 \times 1000 \approx 6.6 \times 10^7$ times of computation. Therefore, we consider sampling just a few of all the pixels for grid search. In our experiment, we first consider sampling one third of the 225 pixels, i.e., 75 pixels or sampling every third pixel, which would compromise the quality of the estimation to some extent, but the computation would be significantly saved as well. In the meantime, we expect that the use of total variation regularization would recover the information on pixels not involved in the grid search, as is clear from the Figures 5.8, 5.9 and 5.10.

Since the value of the residual can be further improved by incorporating the values of pixel estimate as measured by the residual, we do this by weighting those pixels according to the relative quality of the grid search solution versus other pixels. The resulting estimate is shown in Figure 5.11.

Furthermore, we implement this by iteratively checking the pixels with the ten worst least squares pixels, i.e., the 10 largest residuals, to discover the mismatch due to the undersampling and do a grid-search for these pixels again, in order to correct the estimates that deviate too much from the simulated data. The correction is a heuristic which allows us to rectify the severely deviating pixel estimates, as can be seen in Figure 5.12.

5.2.2 The Second Subproblem

We employ a truncated nonlinear conjugate gradient (CG) algorithm (see [Berstekas, 1995]) with a bisection line search to solve this optimization problem.

Starting Point

The quality of the solution depends on the starting point. If a problem has many local minima, the algorithm may converge to a solution other than the desired global optimum. In our experiment, we have two choices of the starting point: the one obtained from the Moore-Penrose pseudo-inverse estimation (tissue quantification problem with homogeneous field), or an arbitrary one. The former starting point is most likely to be close to our solution as demonstrated, so it is a very good starting point.

Thresholding

Since our image has been constructed in such a way that for any pixel, if a specific tissue type exists, then we set 256 for that pixel as image intensity, otherwise 0, we want to set a threshold value for the post-processing of the estimation in order to improve the accuracy of the tissue density estimation. To correct the possible errors in the estimation, we can specify a range so that if the estimate of a tissue type is close to either 256 or 0 with respect to this range, then we assume that there is an error that leads to the deviation, which we need to rectify. We determined empirically that in this case 10 CG iterations and a truncation range of $[-10, 10]$ gave good results for our

simulated problem. The difference between the real tissue density and the estimated tissue density is shown in Figure 5.13.

Note that the thresholding strategy is successful in estimating the tissue densities in a few iterations, since there are just several misestimates in the tissue densities.
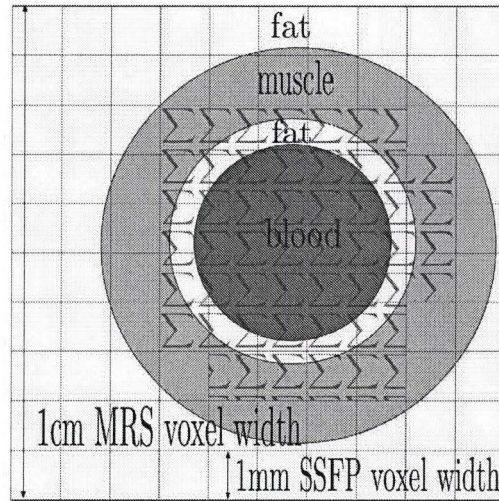

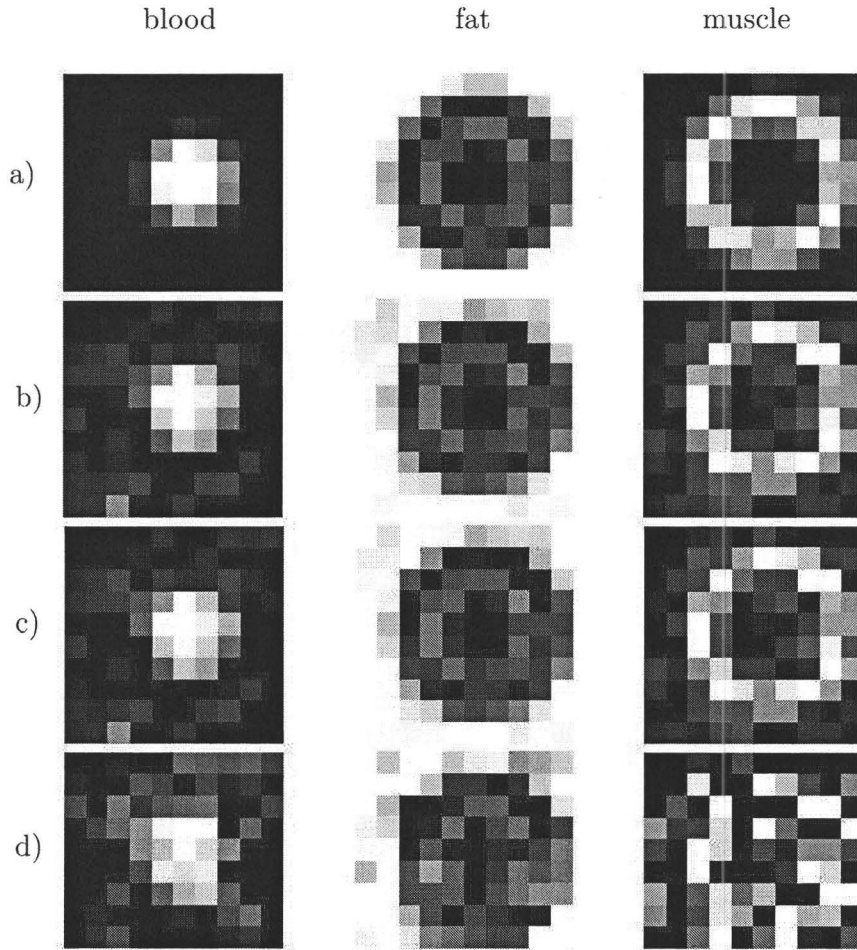Figure 5.1: The cross section of idealized carotid artery.

Figure 5.2: Tissue density reconstruction simulation: each column represents a different tissue, as labelled; ideal (zero noise) tissue densities are shown in row a), densities reconstructed from data collected with the optimal pulse sequence design are in row b), row c) shows the densities from the pulse sequence found by grid search, and row d) illustrates the tissue density estimation based on Dixon method. All values are displayed using the same gray scale.
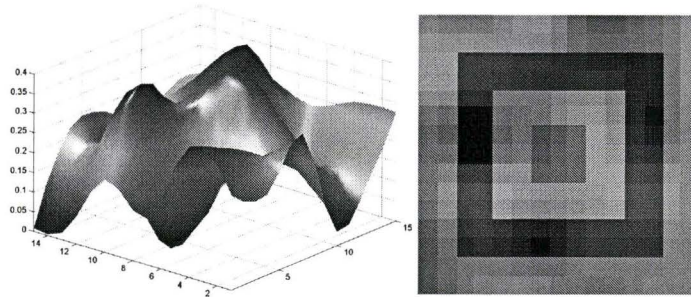
Figure 5.3: The simulated field inhomogeneity from the magnet and tissue susceptibility, respectively.
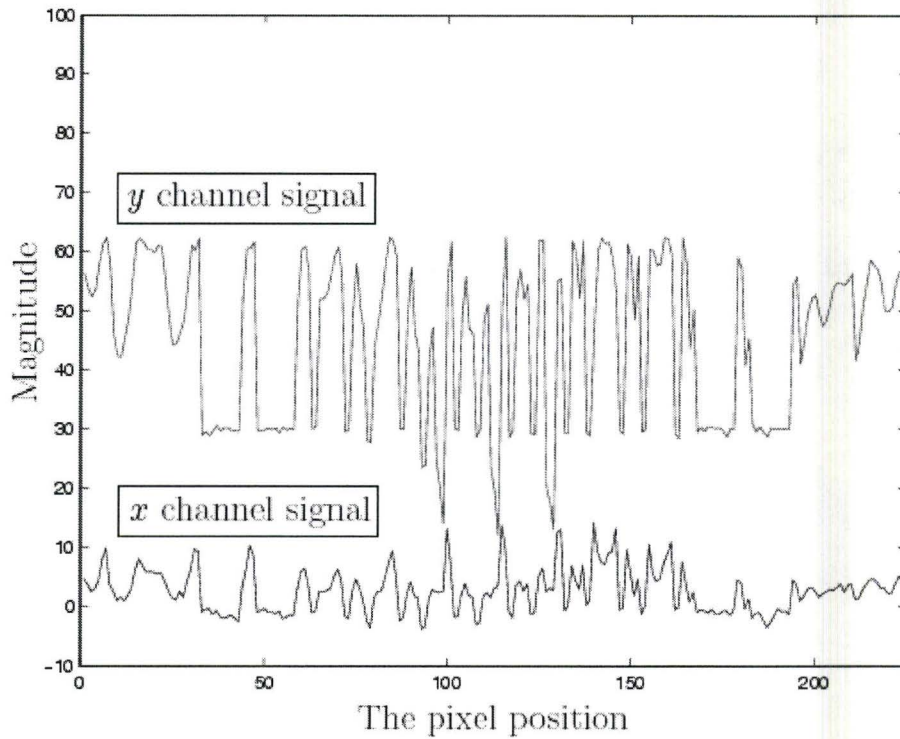
Figure 5.4: The simulated signal from the x and y components (channels) of the magnetization:

52
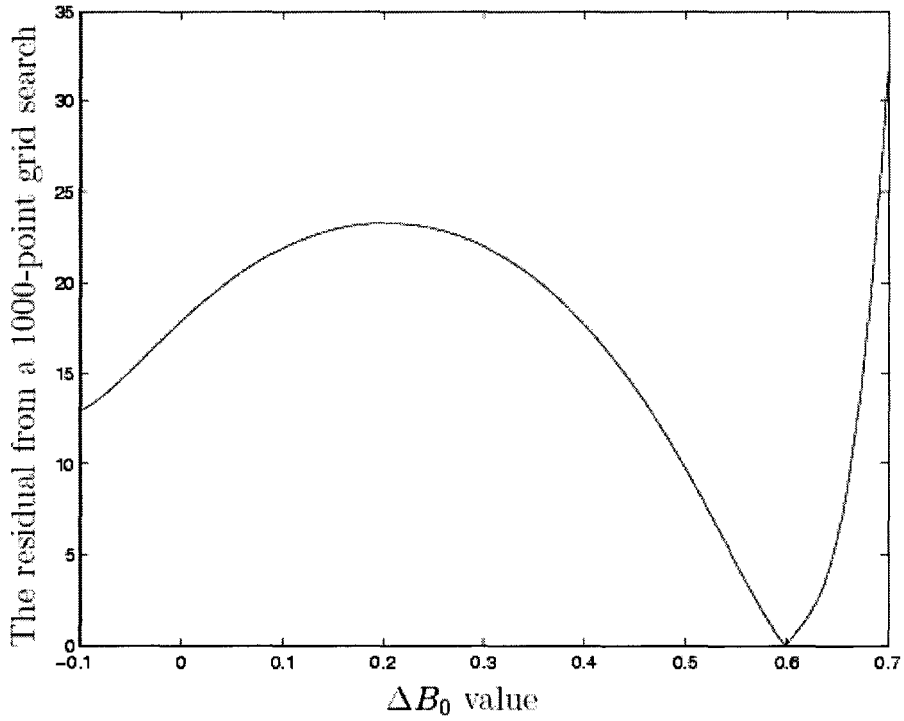
Figure 5.5: The curve represents the residual resulting from a grid search at a specific pixel, with the grid consisting of 1000 points.
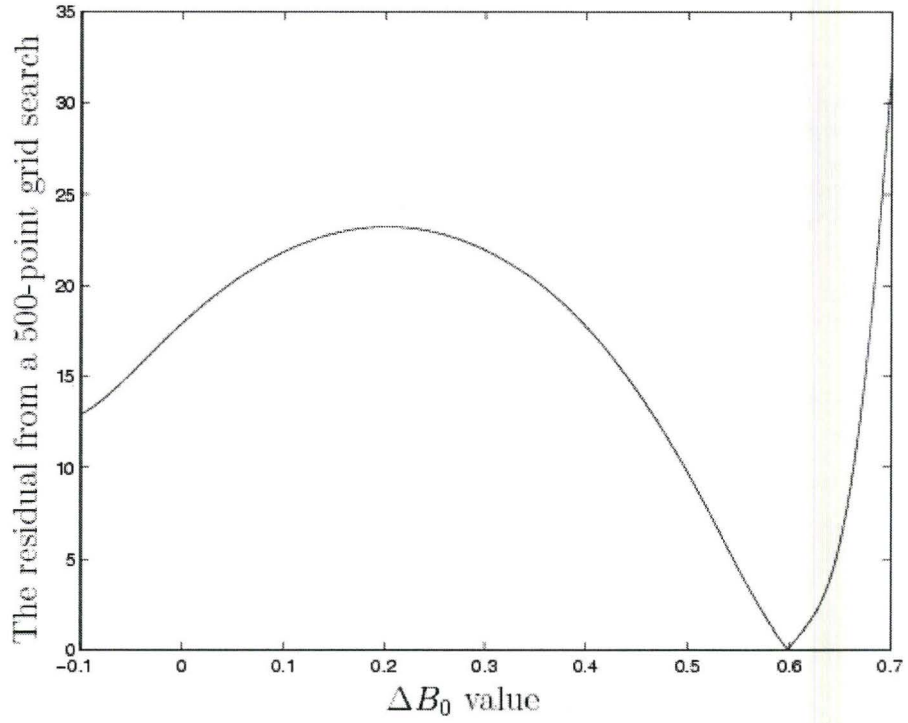
Figure 5.6: The curve represents the residual resulting from a grid search at a specific pixel, with the grid consisting of 500 points.
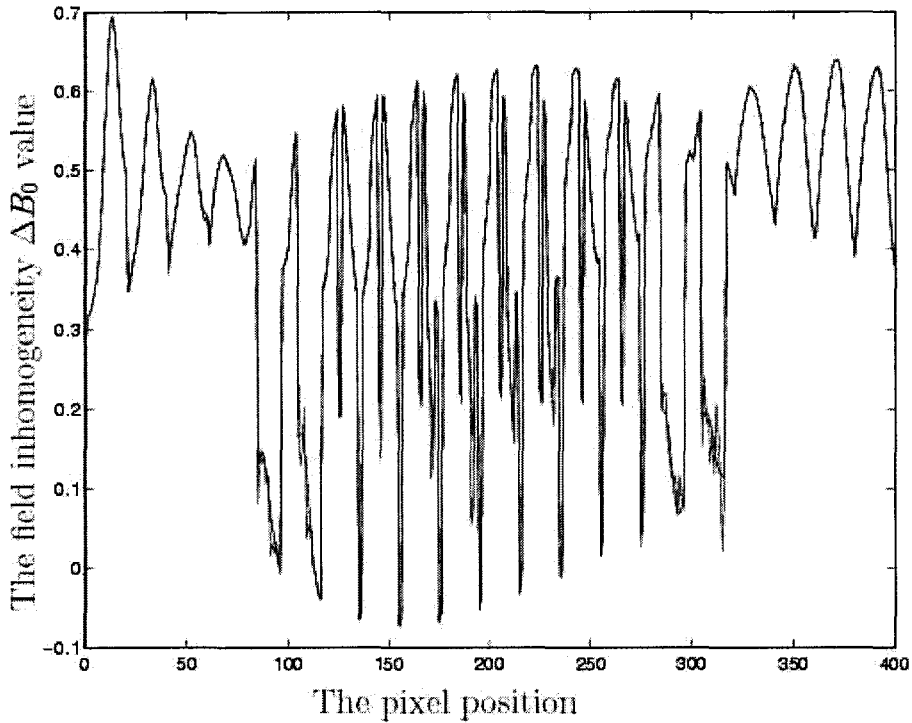
Figure 5.7: The two curves represent the original field inhomogeneity and the solution after the optimization with the starting point from the grid search. As it can be seen from the graph, they match each other very well, except at a few spots.
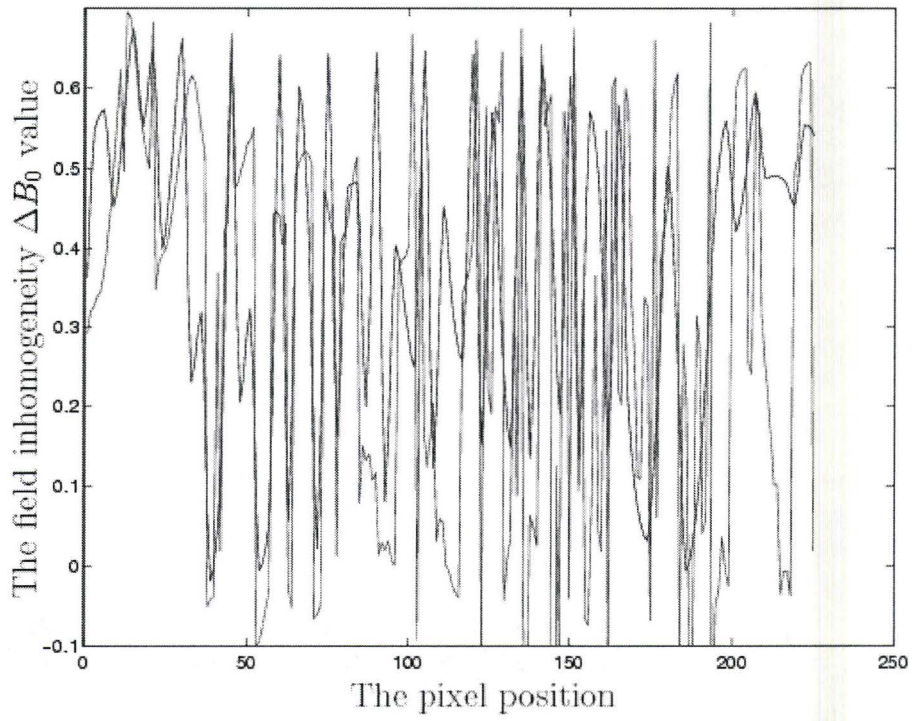
Figure 5.8: Partial grid search based estimation.
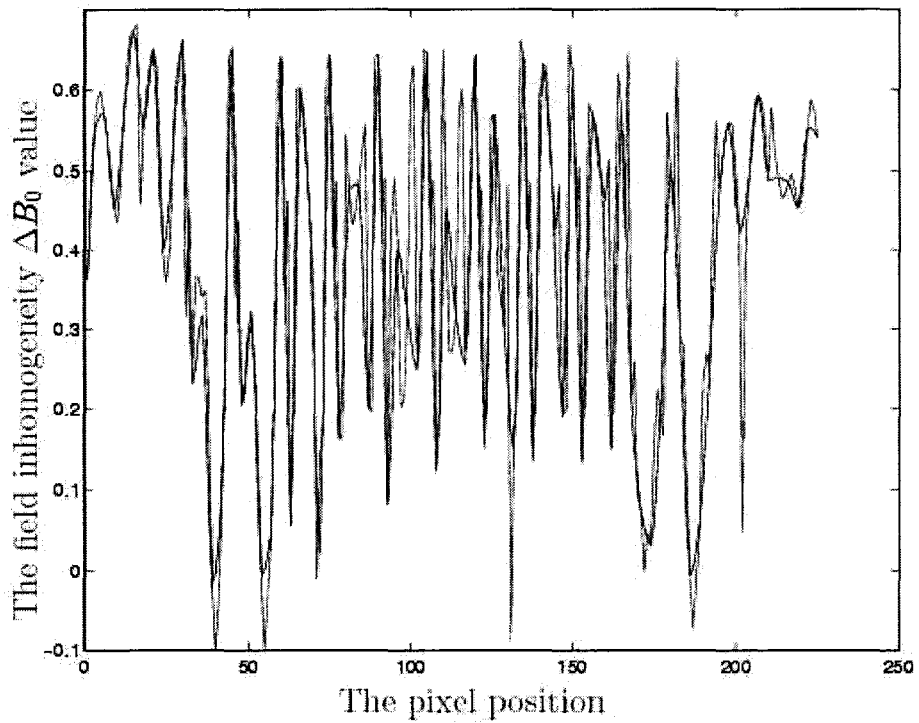
Figure 5.9: Partial grid search followed by total variation regularization estimation.
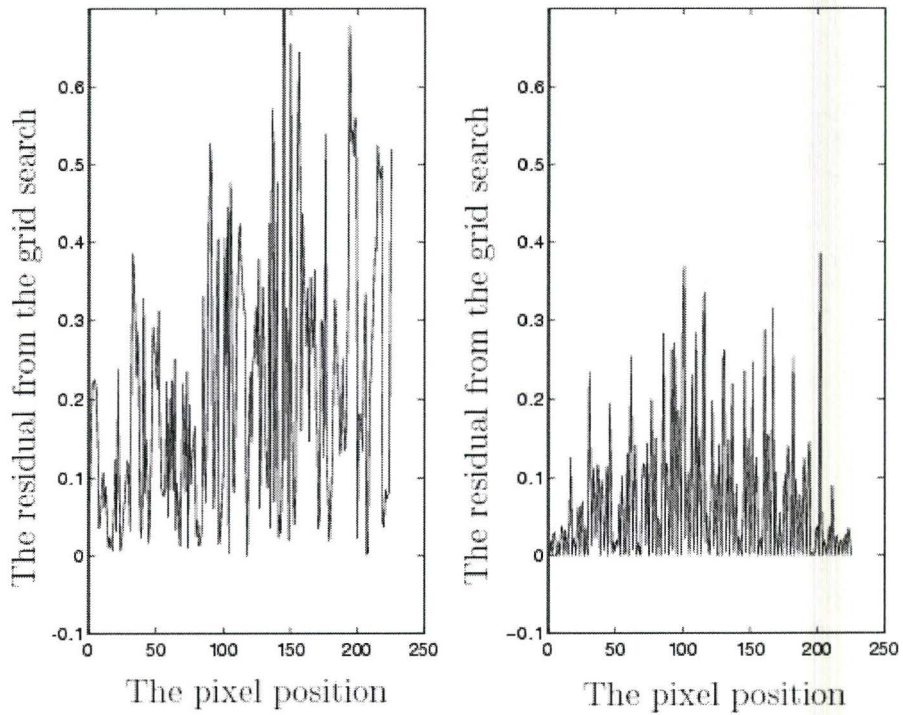
Figure 5.10: The residual curve for, the starting point obtained by the partial grid search (left), and for the starting point obtained by partial grid search followed by total variation regularization (right).
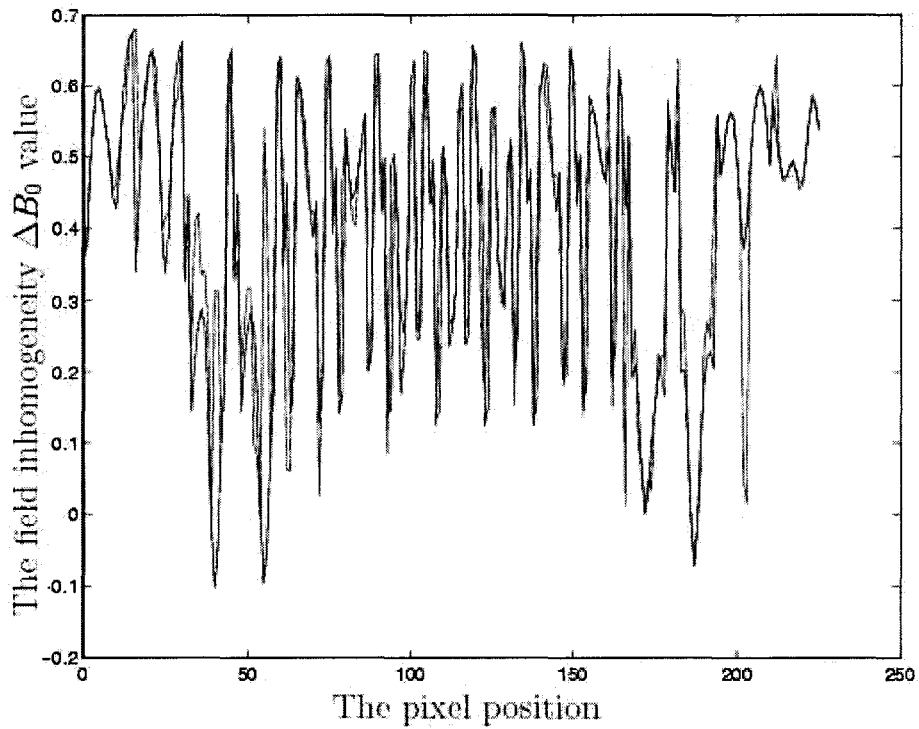
Figure 5.11: Partially sampled pixels for grid search starting point without weighting the residuals.
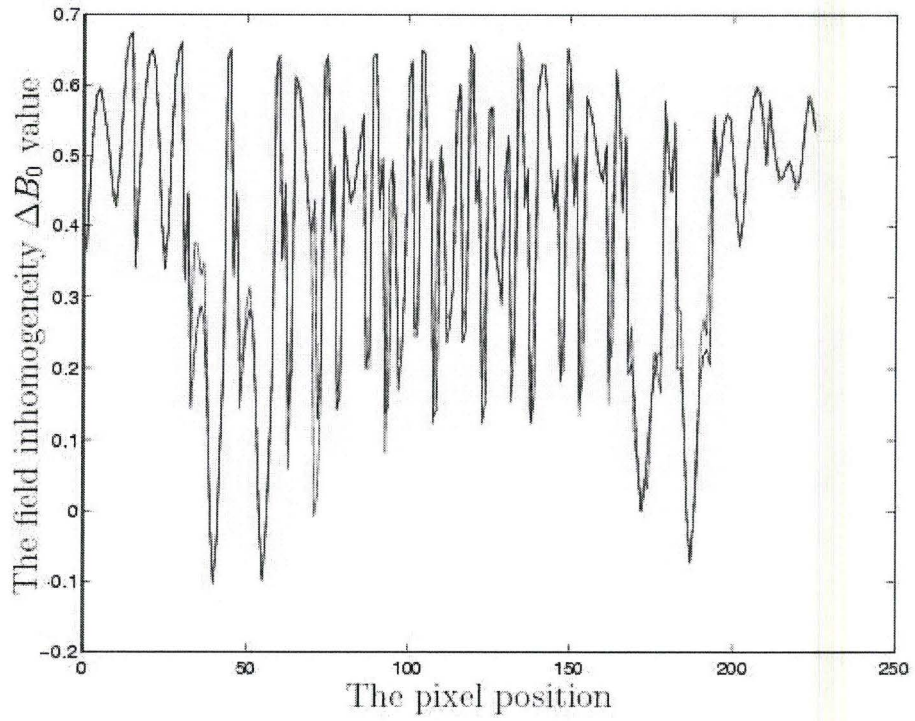
Figure 5.12: Partially sampled pixels for grid search starting point with pixel residuals weights.
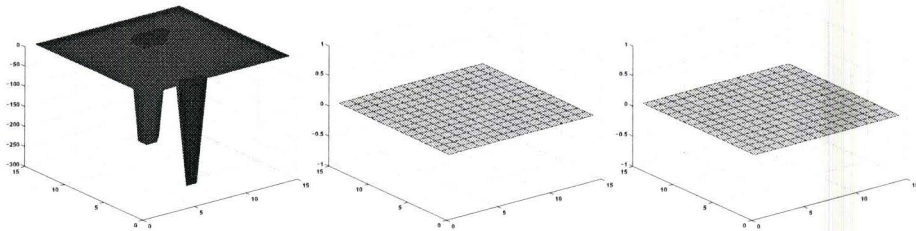
Figure 5.13: The difference between the real tissue density and estimated tissue density for the tissue types: fat, blood, and muscle, respectively (from left to right).

Chapter 6

Conclusions and Future Work

We have modelled SSFP-based tissue quantification, and optimized both the pulse design and density reconstruction phases of the problem to maximize the contrast-to-noise ratio in the resulting tissue densities. We have demonstrated numerically the improvement for carotid artery intraluminal lipid quantification.

This model-based approach is a significant innovation from previous methods, which opens many possible algorithm improvements.

6.1   Pulse Design

We have investigated tissue quantification as a generalization of Dixon's method. We have developed a method for optimal design of SSFP pulse sequences for MR tissue quantification. Our method requires the solution of a nonlinear, nonconvex semi-definite optimization problem. We have shown that generalizing Dixon's method by removing assumptions about the best complex phase relationships between tissue types across multiple images results in dramatically better tissue quantification. The resulting model represents what clinicians and researchers want most: the reduction of error in the calculated tissue quantities. The resulting optimization problem has semi-definite and other highly-nonlinear constraints. We have developed a method for solving it

that combines grid search and a sequential SDO trust-region algorithm. Since we do not obtain conventional Dixon phase relationships for optimizing pulse sequence design variables, we should suspect that conventional Dixon methods are not optimal. More significantly, we have provided computational evidence that our generalized Dixon method produces better results than conventional Dixon method(see Table 5.1).

6.2 Regularized Tissue Density Estimation

We have also studied the case where main magnetic field inhomogeneities exist, by incorporating field inhomogeneity into the tissue quantification process. We have estimated tissue density, as well as field inhomogeneity based on the total variation regularized model, in which we regularize the grid search solution in order to obtain a field inhomogeneity estimate. Then we estimate tissue density based on the ΔB_0 information. Even though the model is highly nonlinear in ΔB_0, numerical results show that total variation regularization works well, and yields good results for both field inhomogeneity and tissue density estimation.

6.3 Applications

Identifying tissue distribution in-vivo has many applications in diagnostic imaging, treatment monitoring, and biological research. In many cases, information about tissue composition may be known from MR spectroscopy, but acquisition times are too long to apply spectroscopy in clinical diagnosis. Since MR does not involve ionizing radiation, it is attractive for population-scale screening. After developing appropriate sequences using our optimization method, it may be cost-effective to do so, *e.g.,* for quantifying liver fat. In a similar way, the reduced imaging time requirements for SSFP-based quantification, will make longitudinal studies feasible, *e.g.,* brain development studies in infants based on white and gray matter quantification. We have clinical partners for one such application and are planning to conduct research in this direction.

6.4 Algorithm Development

In most imaging environments, technicians are free to adjust pulse-sequence design variables to suit the subject (including the subjects ability to remain still). Although our sequential trust-region SDO-SOCO algorithm is very fast, the initial grid search in our algorithm, whose cost grows exponentially with the number of experiments, is simply too slow to be used in this setting. We are exploring several heuristics to find good starting points quickly, even if we are less likely to find the global optimum. We are optimistic about such heuristics, at least in the case of many experiments. We will also investigate including the variables T_l in the subproblems, as a possible way of increasing the basins of convergence (and thus reducing the cardinality of the grid). If these methods are not sufficient, we could always precompute good starting points for ranges of parameters to hide the cost of the grid search from the end user.

We have formulated the parameter selection problem in terms of SSFP imaging. Since different sequence types are sensitive to different tissue properties, one would expect better quantification by looking at mixed imaging, using some SSFP images and some other imaging types, *e.g.*, fast spin echo, spoiled sequences, gradient-reversed fast imaging with steady-state precession, inversion recovery sequences, see Haacke et al. [1999]. There is no fundamental obstacle to formulating mixed imaging parameter selection, but software complexity will increase by having a nonconvex mixed continuous and discrete optimization problem.

In addition to main magnetic field inhomogeneity, we also need to take into account the so-called B_1 field inhomogeneity, resulting from rf coil non-uniformity (introduced in the design or manufacture of coils) and interactions between the generated field and the sample, which grow as the field strength grows. In this thesis, we have shown that by introducing TV-regularization, we are able to recover from B_0 inhomogeneity, and we are confident that in the future the same technique can be applied to the estimation of, and correction for B_1 inhomogeneity, which will be necessary in order to use these techniques at higher field, *e.g.* 3T.

The most challenging area for future investigation is the adaptation of our method to situations in which parameters change between patients and within patients. Not all tissue parameters are accurately known, and some

are known to vary as a function of pH and hydration. For our methods to be applicable in these situations, we will have to develop integrated methods of estimating these parameters–perhaps from the source images as a stage in processing to precede quantification.

Although these issues are challenging, we believe that they are all solvable by adapting known techniques, or by modifying the existing model in ways which change the size (and notational complexity) of the problem, but which do not change its character. Our success in modelling and numerically simulating and solving the tissue quantification problem, therefore, gives us confidence to begin development of a robust implementation.

Appendix A

Algorithms

A.1   A Trust Region Algorithm for NL-SDO

In this section, we explain our algorithm for solving (NL-SDO) where $(T_1, \ldots, T_n)$ and $(t_1, \ldots, t_m)$ are fixed parameters (see Section 2.2). We name the model with fixed T_l and t_k values (NL-SDO), (see page 18). The values of the tissue parameters $(t_1, \ldots, t_m)$ that are used in the algorithm for solving (NL-SDO), are representative values chosen from the literature, and the values of the design variables T_l, $l = 1, \ldots, n$ are obtained by a grid search that is explained in §A.1.2.

Our aim is to solve the nonlinear semidefinite problem (NL-SDO) by solving a sequence of linear mixed semidefinite (SDO) and second order cone (SOCO) trust region subproblems. We chose to fix the values of T_l in the nonlinear problem because the T_l appear in multiple places in the constraints (within both real exponentials and sine and cosine) which come from the dynamical system (1.19), and we couldn't find a suitable change of coordinates (as we did in changing from angles to unit vectors) to reduce the nonlinearity. This decision was supported by subsequent visual exploration of the objective function, which strongly suggested that the objective is 'less convex' and has a larger Lipschitz constant in the T_l directions than the other variable directions. Rapid changes in the objective as a function of the variables T_l is consistent with the inverse relationship between the repeat time and the resonance frequency. More investigation is required to understand the differences in roles of

the pulse sequence design variables, methods such as automatic differentiation are needed to overcome the technical difficulty in treating the T_l variables–and in dealing with many more degrees of freedom, and more complicated pulse design problems. Given the focus of the present paper on demonstrating the validity of the SDO formulation and gauging the difficulty of solution (on a clinically relevant, but relatively simple test problem), we felt it was reasonable to fix the values of T_l in the subproblems.

In this section we first derive a linear mixed SDO and SOCO trust region subproblem (P_{lin}), (see page 68) obtained by linearizing (NL-SDO) with respect to $(u_{1l}, u_{2l}, u_{3l}, u_{4l})$, $l = 1, \ldots, n$, and then explain our sequential SDO trust region algorithm based on (P_{lin}), (see page 68).

A.1.1 Linearization and the SDO-Trust Region Subproblem

It is known that mixed SDO and SOCO problems can be solved efficiently with interior-point methods (IPMs), (see Sturm [2002]). Therefore, for the eigenvalue problem (NL-SDO) we introduce SDO-SOCO subproblems defined on a trust region. The semidefinite eigenvalue constraint

$$S^T S - \lambda I \succeq 0 \tag{A.1}$$

is not fitting in the form of linear conic optimization, therefore we substitute out the quadratic term as $X = S^T S$ and replace constraint (A.1) by the following two constraints

$$\begin{aligned} X &= S^T S \\ X - \lambda I &\succeq 0. \end{aligned}$$

The first constraint is nonlinear while the second one is a standard SDO constraint. By taking into consideration that T_l are *fixed parameters*, we

rewrite (NL-SDO) problem as follows

$$\max \quad \lambda$$

$$
\begin{aligned}
\text{s.t.} \quad & X - \lambda I \succeq 0 \\
& X = S^T S, \\
& A(u_l, t_k) M_{SS}(u_l, t_k) = b(u_l, t_k), \quad \forall l, k \\
& u_{1l}^2 + u_{2l}^2 \leq 1, \quad \forall l \\
& u_{3l}^2 + u_{4l}^2 \leq 1, \quad \forall l,
\end{aligned}
\tag{P}
$$

where $l = 1, \ldots, n$, and $k = 1, \ldots, m$.

Now, we develop a *sequential semidefinite trust-region based algorithm* for solving (NL-SDO). At each iteration we define a linear SDO-SOCO trust region subproblem by linearizing the nonlinear constraint around the current point and restrict the movement to a certain trust region. Our next step is to linearize with respect to $(u_{1l}, u_{2l}, u_{3l}, u_{4l})$, $l = 1, \ldots, n$ the constraint

$$X = S^T S, \tag{A.2}$$

To simplify the notation, we write $X = X(u_1, \ldots, u_n, t_1, \ldots, t_m)$. Each element in matrix S corresponds to x or y component of a steady state magnetization that depends on tissue parameters t_k and design variables u_l, (see 2.9). Therefore, for the linearization of the nonlinear constraint (A.2) we explore the nonlinear constraints

$$A(u_l, t_k) M_{SS}(u_l, t_k) = b(u_l, t_k), \quad l = 1, \ldots, n, \ k = 1, \ldots, m, \tag{A.3}$$

and remove them from the derived conic subproblem. It is easy to see that

$$
\begin{aligned}
X_{pq} &= \sum_{l=1}^{n} S_{lp} S_{lq} \\
&= \sum_{l=1}^{n} (M_{SS,x}(u_l, t_p) M_{SS,x}(u_l, t_q) + M_{SS,y}(u_l, t_p) M_{SS,y}(u_l, t_q)),
\end{aligned}
\tag{A.4}
$$

and

$$
\begin{aligned}
\frac{\partial X_{pq}}{\partial u_{jl}} =\ & \frac{\partial M_{SS,x}(u_l, t_p)}{\partial u_{jl}} M_{SS,x}(u_l, t_q) + M_{SS,x}(u_l, t_p) \frac{\partial M_{SS,x}(u_l, t_q)}{\partial u_{jl}} \\
& + \frac{\partial M_{SS,y}(u_l, t_p)}{\partial u_{jl}} M_{SS,y}(u_l, t_q) + M_{SS,y}(u_l, t_p) \frac{\partial M_{SS,y}(u_l, t_q)}{\partial u_{jl}},
\end{aligned}
\tag{A.5}
$$

67

where $p, q = 1, \ldots, m$, $j = 1, \ldots, 4$, $l = 1, \ldots, n$. In point (u_l, t_k) the values of steady state magnetization and the corresponding partial derivatives are computed from (A.3), and

$$A(u_l, t_k) \frac{\partial M_{SS,x}(u_l, t_k)}{\partial u_{jl}} = \frac{\partial b(u_l, t_k)}{\partial u_{jl}} - \frac{\partial A(u_l, t_k)}{\partial (u_l)_j} M_{SS,x}(u_l, t_k), \qquad \text{(A.6)}$$

respectively, where $k = 1, \ldots, m$, $M_{SS,x}(u_l, t_k) = (M_{SS}(u_l, t_k))_1$, and $M_{SS,y}(u_l, t_k) = (M_{SS}(u_l, t_k))_2$. Since $A(u_l, t_k)$ is nonsingular (see page 8), we can always solve for $M_{SS}(u_l, t_k)$ and $\partial M_{SS}(u_l, t_k)/\partial u_{jl}$ in (A.3) and (A.6). These values are then used for computing (A.4) and (A.5) that are explored further in linearization.

Let $h_l = (h_{1l}, h_{2l}, h_{3l}, h_{4l}, h_{5l}) \in R^5$ denote the displacement in u_l for $l = 1, \ldots, n$. Since in problem (P) parameters T_l are fixed, it follows that $h_{5l} = 0$ for all l. Now, from (A.4)–(A.6) we derive the first order approximation of the nonlinear constraint (A.2), *i.e.*,

$$X(u_1 + h_1, \ldots, u_n + h_n, t_1, \ldots, t_m)_{p,q} = X_{pq} + \sum_{l=1}^{n} h_l^T \nabla_{u_l} X_{pq}. \qquad \text{(A.7)}$$

Finally, by using (A.7) we derive the following problem that is obtained by linearizing (P) around the point $(u_1, \ldots, u_n)$, where T_l are fixed, and with respect to the trust region radius Δ:

$$
\begin{aligned}
\text{max} \quad & \lambda \\
\text{s.t.} \quad & X_{\text{lin}} - \lambda I \succeq 0 \\
& (X_{\text{lin}})_{pq} = X(u_1 + h_1, \ldots, u_n + h_n, t_1, \ldots, t_m)_{pq}, \quad \forall p, q \\
& X \succeq 0 \qquad\qquad\qquad\qquad\qquad\qquad\qquad\qquad\qquad (\text{P}_{\text{lin}}) \\
& (u_{1l} + h_{1l})^2 + (u_{2l} + h_{2l})^2 \leq 1, \quad \forall l \\
& (u_{3l} + h_{3l})^2 + (u_{4l} + h_{4l})^2 \leq 1, \quad \forall l \\
& \sum_{l=1}^{n} \sum_{j=1}^{4} h_{jl}^2 \leq \Delta^2,
\end{aligned}
$$

where $p, q = 1, \ldots, m$, $l = 1, \ldots, n$, and $X(u_1 + h_1, \ldots, u_n + h_n, t_1, \ldots, t_m)_{p,q}$ is computed as in (A.7). Note that the trust region constraint is a second order cone constraint, and therefore the optimization problem (P_{lin}) is a

linear mixed SDO-SOCO problem. Note that we do not need to linearize the constraints (A.3) for S, because S can be effectively computed as a function of the variables u_l. If S were *only* defined by the constraints, we would have to linearize those constraints and project the solution of the linear subproblem onto the constraint manifold. Direct computation reduces the size of the linear subproblem and eliminates the projection step, see Section ?? for further details.

Problem (P_{lin}) is the *trust region subproblem* in the algorithm that is described in the following subsection. We use the optimization software SeDuMi Sturm [1999] for solving these subproblems.

A.1.2   The Algorithm

Here we describe our trust-region based algorithm that solves (P), (see page 67). Problem (P) is a nonconvex problem and the algorithm converges to a local optimum. We ensure that the point computed by the algorithm is at least a local optimum of (P), by numerically verifying the Karush-Kuhn-Tucker conditions at that point. The algorithm is iterative and maintains at each iteration a feasible current point and the solution of the linearized model in it. It also maintains the smallest eigenvalue of $S^T S$ where S is computed at the current point.

Grid search to fix T_l and the Starting Point. Although we can start the algorithm from any feasible point of (NL-SDO), (see page 18), a grid search is developed for finding a "good" initial point and to find good T_l values, that are fixed for the rest of the algorithm. Note that in model (NL-SDO), T_l, $l = 1, \ldots, n$ are variables. We form a grid with respect to (α_l, f_l, T_l), $l = 1, \ldots, n$, and compute S at each point of that grid. The "best" point obtained by the grid search, is the one with the property that the smallest eigenvalue of $S^T S$ is the largest, among smallest eigenvalues of the matrices $S^T S$ at different grid points. The values for T_l from the "best" grid point, are now fixed parameters in the algorithm for solving (NL-SDO). The values for (α_l, f_l), $l = 1, \ldots, n$ at the "best" grid point, are the starting values of the algorithm. Our numerical experiments justify this choice of starting point (see Section ??).

Note that the quality of the "best" initial point in the described way,

depends on the density of the grid. Namely, the denser the grid, the "better" starting point is computed. However, the cost of the grid search increases exponentially with the number of the experiments n in the model and/or the grid density.

We denote now the initial point obtained from the grid search, by $(u_1^0, \ldots, u_n^0, t_1, \ldots, t_m)$, and the smallest eigenvalue of $(S^0)^T S^0$ by λ^0. Note that the input values T_l^0 are fixed during the optimization algorithm. We specify the *initial trust region radius, e.g.,* $\Delta^0 := 1$.

General step. To describe a general step of the algorithm, we assume to have a *current feasible point* $(u_1, \ldots, u_n, t_1, \ldots, t_m)$. Let the value of the objective function in the current point be $\bar{\lambda}$, which is the smallest eigenvalue of $S^T S$. The minimization of (P_{lin}), (see page 68) around the current point with respect to the corresponding trust region radius Δ gives a *new candidate point* $(u_1 + h_1^*, \ldots, u_n + h_n^*)$, and the corresponding value of the objective function λ^*. Note that the new candidate point will satisfy (A.3) due to the construction of the algorithm, *i.e.,* by solving (A.3) for $M_{SS}(u_l, t_k)$ at each iterate. Therefore the feasibility of each iterate is ensured. More precisely, the steps in the algorithm are

$$h^* \rightarrow u + h^* \rightarrow (\text{from}(A.3)) \ \ M(u + h^*, t) \rightarrow (\text{from } (P_{\text{lin}})) \ \lambda^*.$$

We denote by $\hat{\lambda}^*$ the smallest eigenvalue of $S^T S$, where S is computed at the new candidate point. Then we compute the *trust region ratio* ϱ based on the information of the new candidate point, *i.e.,*

$$\varrho = \frac{\bar{\lambda} - \hat{\lambda}^*}{\bar{\lambda} - \lambda^*}. \tag{A.8}$$

Note that the closer the value of ϱ is to one, the better approximation by the linearized model is realized. If a sufficient reduction at the objective function is obtained at the candidate point, then that point is accepted as the next iterate and the trust region radius is expanded or kept the same, as specified by (A.9). A negative or very small ϱ indicates a poor approximation, and therefore the point is rejected and the trust region radius is reduced. More precisely, we update the *trust region radius* Δ, (see *e.g.,* Berstekas [1995]; Conn et al. [2000]), in the following way:

$$\Delta^* = \begin{cases} c_1 \Delta, & \text{if } \varrho < r_1 \\ c_2 \Delta, & \text{if } \varrho > r_2 \\ \Delta, & \text{otherwise.} \end{cases} \tag{A.9}$$

In our computations we set $c_1 = 0.25, c_2 = 2$ and $r_1 = 0.2$, $r_2 = 0.95$. The choice of these parameters is made after extensive testing and benchmarking.

Stopping criteria. Several conditions are used for terminating the algorithm. When the trust region becomes very small (*e.g.*, $\leq 10^{-8}$), or too large (*e.g.*, $> 4\Delta^0$) and there is no significant improvement in the objective, we stop the algorithm. Another criterion is when after a pre-specified number of iterations there is no improvement with respect to the objective. We stop the algorithm if the total number of iterations reaches 25.

Finally, we present our sequential SDO-trust-region algorithm for solving problem (P), by the pseudo code in Figure A.1.2.

Algorithm I

Input:

    tissue parameters: $t_k = (\tau_{1k}, \tau_{2k}, \kappa_k)$, $\quad k = 1, \ldots, m$;

    repetitive time parameters: T_l^0, $\quad l = 1, \ldots, n$;

    initial design variables: (α_l^0, f_l^0), $\quad l = 1, \ldots, n$;

    compute: $u_l^0 = (\cos(\alpha_l^0), \sin(\alpha_l^0), \cos(f_l^0), \sin(f_l^0), T_l^0)$, $\quad l = 1, \ldots, n$;

    initial trust region radius: $\Delta^0 = 1$;

    input parameters: $r_1 = 0.25, r_2 = 2, c_1 = 0.2, c_2 = 0.95$;

begin

    $\Delta \leftarrow \Delta^0$;

    $u_l \leftarrow u_l^0$, $\quad l = 1, \ldots, n$;

    while one of the stopping criteria is satisfied (see page 71)

        solve (P_{lin}), (see page 68) $\rightsquigarrow$ optimal value λ^*, h_l^*, $l = 1, \ldots, m$;

        new candidate point: $u_l^* = u_l + h_l^*$, $\quad l = 1, \ldots, n$;

        compute ρ from (A.8);

        if $\varrho < r_1$

           reduce Δ;

        else

           update Δ according to (A.9)

           $u_l \leftarrow u_l^*$, $\quad l = 1, \ldots, n$;

        end

    end

    return (α_l, f_l), $\quad l = 1, \ldots, n$ and $\hat{\lambda}^*$;

end

Figure A.1: Sequential, trust-region, second-order conic algorithm.

Bibliography

A. Albert, "Conditions for positive and nonnegative definiteness in terms of pseudoinverses," *SIAM Journal on Applied Mathmatics*, vol. 17, pp. 434–440, 1969.

A. Ben-Tal and A. Nemirovski, *Lectures on Modern Convex Optimization. Analysis, Algorithms and Engineering Applications*, vol. 1 of MPS/ SIAM Series on Optimization, SIAM, Philadelphia, U.S.A., 2001.

D.P. Berstekas, *Nonlinear Programming*. Athena Scientific, U.S.A., 1995.

H.Y. Carr, "Steady-state free precession in nuclear magnetic resonance," *Physics Review*, vol. 112, pp. 1693-1701, 1958.

C.E. Coffey, W.E. Wilkinson, and I.A. Parashos, "Quantitative cerebral anatomy of the aging human brain: a cross-sectional study using magnetic resonance imaging", *Neurology*, vol. 42, pp. 527–536, 1992.

A.R. Conn, N.I.M. Gould, and P.L. Toint, *Trust Region Methods*. MPS–SIAM Series on Optimization, 2000.

W.T. Dixon, "Simple proton spectroscopic imaging," *Radiology*, vol. 153, pp. 189–194, 1984.

G. Glover, "Multipoint Dixon technique for water and fat proton and susceptibility imaging," *Journal of Magnetic Resonance Imaging*, vol. 1, pp. 521–530, 1991.

E.M. Haacke, R.W. Brown, M.R. Thompson, and R. Venkatesan, *Magnetic Resonance Imaging, Physical Principles and Sequence Design*. Wiley-Liss, 1999.

W. Hanicke and H.U. Vogel, "An analytical solution for the SSFP signal in MRI," *Magnetic Resonance in Medicine*, vol. 49, pp. 771–775, 2003.

P.C. Hansen, *Computational Inverse Problems in Electrocardiology.* WIT Press, 2001.

B.A. Hargreaves, S.S. Vasanawala, J.M. Pauly, and D.G. Nishimura, "Characterization and reduction of the transient response in steady-state MR imaging," *Magnetic Resonance in Medicine*, vol. 46, pp. 149–158, 2001.

B.A. Hargreaves, S.S. Vasanawala, K.S. Nayak, J.H. Brittain, B.S. Hu, and D.G. Nishimura, "Fat-suppressed steady-state free precession imaging using phase detection," *Magnetic Resonance in Medicine*, vol. 50, pp. 210–213, 2003.

R.A. Horn and C.R. Johnson, *Matrix Analysis.* Cambridge University Press, Cambridge, UK, 1985.

T.Y. Huang, H.W. Chung, F.N. Wang, C.W. Ko, and C.Y. Chen, "Fat and water separation in balanced steady-state free precession using the Dixon method," *Magnetic Resonance in Medicine*, vol. 51, pp. 243–247, 2004.

S. Jardim and M. Figueiredo, "Automatic contour estimation in fetal ultrasound images," *IEEE International Conference on Image Processing - ICIP'2003*, Barcelona, Spain, September 2003.

P.C. Lauterbur, "Image formation by induced local interactions: Examples employing NMR," *Nature*, vol. 242, pp. 190–191, 1973.

Y.Y. Li and F. Santosa, "A computational algorithm for minimizing total variation in image restoration", *IEEE Transactions on Image Processing*, vol. 5, pp. 987–995, 1996.

W. Li, P. Storey, Q. Chen, S.Y. Li, V. Prasad, and R. Edelman, "Dark flow artifacts with ateady-State free precession cine MR technique: causes and implications for cardiac MR imaging," *Radiology*, vol. 230, pp. 569-575, 2004.

Z.P. Liang and P.C. Lauterbur, *Principles of Magnetic Resonance Imaging*, IEEE Press Series in Biomedical Engineering, 1999.

P. Mansfield and P.K. Grannell, "NMR 'diffraction' in solids?," *Journal of Physics C: Solid State Physics*, vol. 6, pp. 422–426, 1973.

K.V. Mardia, J.T. Kent, and J.M. Bibby, *Multivariate Analysis*, Academic Press, 1979.

K.S. Nayak and D.G. Nishimura, "Automatic field map generation and off-resonance correction for projection reconstruction imaging," *Magnetic Resonance in Medicine*, vol. 43, pp. 151–154, 2000.

S.B. Reeder, Z.F. Wen, H.Z. Yu, A.R. Pineda, G.E. Gold, M. Markl, and N.J. Pelc, "Multicoil Dixon chemical species separation with an iterative least-squares estimation method," *Magnetic Resonance in Medicine*, vol. 51, pp. 35–45, 2004.

L. Rudin, S. Osher, and E. Fatemi, "Nonlinear Total Variation based noise removal algorithms," *Physica D*, vol. 60, pp. 259–268, 1992.

F.J. Rybicki, R.V. Mulkern, R.L. Robertson, C.D. Robson, T. Chung, and J. Ma, "Fast three-point Dixon MR imaging of the retrobulbar space with low-resolution images for phase correction: comparison with fast spin-echo inversion recovery imaging," *American Journal of Neuroradiology*, vol. 22, pp. 179–1802, 2001.

N. Salibi and M.A. Brown, *Clinical MR Spectroscopy: First Principles*. Wiley-Liss, New York, 1998.

P. Santago and H.D. Gage, "Quantification of MR brain images by mixture density and partial volume modeling," *IEEE Transactions on Medical Imaging*, vol. 12, pp. 566–574, 1993

K. Scheffler, "On the transient phase of balanced SSFP sequences," *Magnetic Resonance in Medicine*, vol. 49, pp. 781–783, 2003.

J.F. Sturm, "Using SeDuMi 1.02, a MATLAB toolbox for optimization over symmetric cones," *Optimization Methods and Software*, vol. 11-12, pp. 625–653, 1999.

J.F. Sturm, "Implementation of interior point methods for mixed semidefinite and second order cone optimization problems," *Optimization Methods and Software*, vol. 17(6), pp. 1105–1154, 2002.

A.N. Tikhonov and V.Y. Arsenin, *Solutions of Ill-Posed Problems*. Wiley-Liss, New York, 1977.

S.S. Vasanawala, J.M. Pauly, and D.G. Nishimura, "Linear combination steady-state free precession MRI," *Magnetic Resonance in Medicine*, vol. 43, pp. 82–90, 2000.

C. Vogel, and M. Oman, "Iterative methods for total variation denoising", *SIAM Journal on Scientific Computing*, vol. 17, pp. 227–238, 1996.

Y. Wang, T. Adali, S.Y. Kung, and Z. Szabo, "Quantification and segmentation of rrain tissues from MR images: A probabilistic neural network approach," *IEEE Transactions on Image Processing*, vol. 7, pp. 1165–1181, 1998.

D. Zwillinger, *Handbook of Differential Equation, 3rd ed.*, Boston, MA, U.S.A., Academic Press, 1997.